JOURNAL OF PETROLOGY | VOLUME 45 | NUMBER 2 | PAGES 275–298 | 2004 | DOI: 10.1093/petrology/egg089

Rheological Properties of Partially Molten Lherzolite

MARK E. ZIMMERMAN* AND DAVID L. KOHLSTEDT

DEPARTMENT OF GEOLOGY AND GEOPHYSICS, PILLSBURY HALL, UNIVERSITY OF MINNESOTA, MINNEAPOLIS, MN 55455, USA

RECEIVED NOVEMBER 15, 2002; ACCEPTED JULY 21, 2003

Lherzolite samples synthesized from fine-grained powders prepared from a natural xenolith were deformed at $P = 300\ MPa$ *and* $1373 \leq T \leq 1573\ K$ *in a high-resolution gas-medium deformation apparatus. Below and above the solidus of* $T_s \approx 1433\ K$*, fine-grained lherzolite exhibits a transition from diffusional creep at low stress to dislocation creep at high stress. The transition occurs at a differential stress* $\sigma \approx 100\ MPa$ *in samples with a grain size* $d \approx 20\ \mu m$ *and a melt fraction* $\varphi \approx 0{\cdot}03$*. Extrapolation to upper-mantle conditions suggests that a similar transition will occur in the mantle for* $d = 2\ mm$ *at* $\sigma \approx 0{\cdot}5\ MPa$*. Therefore, both creep mechanisms are likely to contribute to deformation of partially molten regions of the mantle. We determined an empirical relationship for the dependence of strain rate* $\dot{\varepsilon}$ *on* φ *using data for melt-free olivine, analysis of the subsolidus and hypersolidus creep behavior of lherzolite and constraints on* $\varphi(T)$ *from our experimentally determined melting curve. We find that* $\dot{\varepsilon}_\varphi$ *increases approximately exponentially with increasing* φ *in both the diffusional and dislocation creep regimes. The observed enhancement in* $\dot{\varepsilon}_\varphi$ *as a result of melt is much larger than anticipated based on deformation models that consider only an isotropic distribution of melt in triple junctions and do not incorporate the presence of melt along some grain boundaries and the melt preferred orientation that develops during deformation. The results for lherzolite are similar to results reported previously for olivine plus basaltic melt samples, indicating a minor effect of pyroxene content for deformation of partially molten peridotites. Our constitutive equation provides a basis for modeling geodynamic processes in the partially molten mantle beneath mid-ocean ridges and in the mantle wedge above subducting slabs.*

KEY WORDS: *ophiolite; peridotite; upper mantle; mid-ocean ridge; partial melt; deformation mechanism; diffusional creep; dislocation creep; grain boundary sliding; experimental studies; fine-grained materials*

INTRODUCTION

Plate tectonics provides not only the framework for understanding crustal processes that occur at plate boundaries, but also the context for comprehending large-scale mass transport in deeper portions of the Earth that are not directly accessible. New crustal material is created at spreading plate boundaries and recycled into the Earth's interior at subduction zones where plates collide. Recycling of the lithosphere requires convection of some portion of the Earth's mantle and, therefore, at the pressure and temperature conditions known to exist in the mantle, plastic deformation of the convecting rocks must occur. The upper mantle is composed mostly of olivine and pyroxene generally in roughly the same proportions as in lherzolite (Ringwood, 1975). The creation of new crustal material at mid-ocean ridge spreading centers and the existence of basaltic volcanism on the Earth for at least 3·6 billion years (e.g. Hamilton *et al.*, 1983; Hess, 1989) indicate that deformation of partially molten lherzolite has occurred throughout most of the Earth's history. Previous studies of melt segregation and distribution further suggest that partially molten regions exist beneath mid-ocean ridges over long periods of time (Arzi, 1978; Waff & Bulau, 1979; Stolper *et al.*, 1981). Knowledge of the rheological behavior of lherzolite, with and without melt, is therefore essential for understanding the dynamics of mantle flow.

The principal objective of this study is to investigate the flow properties of lherzolite at sufficiently high confining pressures to suppress brittle processes, and at subsolidus and hypersolidus temperatures in order to determine the effect of partial melting on the mechanical behavior of the upper mantle. Very few reliable studies have been performed on polyphase upper-mantle compositions such as lherzolite, which

*Corresponding author. Telephone: 612-626-0572. Fax: 612-625-3819. E-mail: zimme030@umn.edu

contains a high modal abundance of pyroxene (Goetze, 1977; Bussod & Christie, 1991). However, extensive experimental investigations of olivine and olivine with a basaltic melt provide a strong basis for comparison with our study (e.g. Cooper & Kohlstedt, 1984; Beeman & Kohlstedt, 1993; Hirth & Kohlstedt, 1995*a*, 1995*b*).

Extrapolation of the results of laboratory experiments to deformation conditions within the Earth's upper mantle requires that the deformation mechanisms operating in the laboratory experiments are the same as those operating in the Earth. The rheological behavior of a partially molten aggregate is generally classified into three categories: (1) fracture and/or cataclastic flow under unconfined conditions or zero effective pressure (Brace & Riley, 1972; Paterson, 1978; Wendt *et al*., 1998); (2) dislocation creep of the crystalline matrix with and without accommodation by interphase boundary sliding (Chopra & Paterson, 1981; Hirth & Kohlstedt, 1995*b*); (3) grain boundary sliding combined with diffusional creep enhanced by diffusion through the melt phase (Cooper & Kohlstedt, 1984; Hirth & Kohlstedt, 1995*a*). Although these mechanisms may operate simultaneously, in general one mechanism will dominate the deformation kinetics for a particular combination of stress, grain size and temperature, as well as melt fraction, melt composition and melt distribution. The high temperatures, fine grain sizes and low differential stresses used in this high-pressure study permit exploration of the deformation mechanisms described in categories (2) and (3) above.

THEORETICAL FRAMEWORK

Experimental studies performed on single crystals as well as synthetic and natural aggregates provide constraints for developing a theoretical framework for understanding the flow of mantle rocks. The high-temperature ($T/T_m > 0{\cdot}6$, where T_m is melting temperature) creep properties of crystalline materials are generally investigated with reference to a steady-state power-law flow equation of the form

$$\dot{\varepsilon}_{\varphi=0} = \dot{\varepsilon}_o \left(\frac{\sigma}{\mu}\right)^n \left(\frac{b}{d}\right)^p f_{O_2}^m a_{SiO_2}^q \exp\left(-\frac{E^* + PV^*}{RT}\right) \quad (1)$$

describing the creep rate $\dot{\varepsilon}_{\varphi=0}$ for a dry, melt-free sample in terms of the applied differential stress σ, the imposed temperature T and pressure P, and the specified grain size d. Here, φ is the melt fraction, $\dot{\varepsilon}_0$ is a material-dependent parameter, μ is the shear modulus [here taken as 61 GPa, the value for olivine at 1473 K from Webb (1989)], b is the length of the Burgers vector [here taken as 0·475 nm for $b = [100]$ for olivine from Deer *et al*. (1992)], n is the stress exponent, p is the grain-size exponent, E^* is the activation energy for creep, V^* is the activation volume for creep, and R is the gas constant. The dependence of creep rate on oxygen fugacity f_{O_2} and the activity of silica a_{SiO_2} will not be considered in detail in this paper. The mineral assemblage fixes the activity of silica. The oxygen fugacity is set by oxidation of the metal sleeve used to contain the sample, fixing it for a constant-temperature experiment at a value determined by the metal–metal-oxide buffer. The oxygen fugacity exponent in equation (1) varies from $m = 0$ for single crystals of olivine oriented for slip on the hard slip system (Bai *et al*., 1991), to $m \approx 1/6$ for olivine plus basalt deformed at 0·1 MPa (Kohlstedt *et al*., 2002), to $m \approx 1/3$ for polycrystalline olivine deformed at 300 MPa (Beeman & Kohlstedt, 1993).

Reviews of the steady-state creep activation parameters and rate-limiting mechanisms appear elsewhere (e.g. Goetze, 1978; Tullis, 1979; Kirby, 1983; Kirby & Kronenberg, 1987; Kohlstedt, 1992; Evans & Kohlstedt, 1995; Kohlstedt *et al*., 1995). Current estimates of the activation volume for dislocation creep of olivine range from 14 to 27 cm^3/mol (e.g. Karato, 1998; Z. Y. Wang *et al*., in preparation). Because all of our experiments were carried out at $P = 300$ MPa, the PV^* term in equation (1) is small, $\leq 2\%$ of E^*; therefore, the activation energy measured during creep will be represented here as $Q\,(= E^* + PV^*)$. In addition, Q also includes the temperature dependence of the shear modulus, which results in a correction of $< 1\%$ over the temperature range of our experiments. The values of the exponents n and p are indicative of the rate-controlling creep process. Specifically, $n = 1$ if diffusional creep (i.e. grain boundary sliding accommodated by diffusive processes) dominates the deformation, and $p = 1$, 2 or 3 when interface reactions, lattice diffusion or grain boundary diffusion, respectively, controls the creep rate (Nabarro, 1948, 1967; Herring, 1950, 1951; Coble, 1963; Lifshitz, 1963; Raj & Ashby, 1971). If dislocation processes control the creep rate, $n = 3$ to 5 and $p = 0$ (Weertman, 1972). If grain boundary sliding is accommodated by the motion of dislocations into and along the boundary, then $n = 2$ to 3 and $p = 2$ to 1 (Langdon, 1994).

During dislocation creep the grains undergo approximately the same deformation as the polycrystalline rock as a whole, provided that no large disparities exist between the strengths of different phases, that a sufficient number of slip systems are available, and that grain boundary sliding does not occur. The von Mises compatibility condition, which requires five independent slip systems for homogeneous, constant volume deformation, may be relaxed to three if glide and climb of dislocations on all three systems take place simultaneously (e.g. von Mises, 1928; Groves & Kelly, 1968; Paterson, 1969; Dieter, 1976). The von Mises requirement may be relaxed further if other accommodation processes contribute sufficiently. For example, the bulk

of the strain can be attained by intra-crystalline plastic deformation, rate limited by glide or climb on an appropriate slip system, with some grain-to-grain realignment accomplished by grain boundary sliding. Inhomogeneous intra-crystalline deformation, such as the formation of kink bands, may also relax the von Mises requirement. In diffusional creep, adjustments at grain boundaries must occur to maintain strain compatibility between adjoining grains, requiring grain boundary and phase boundary sliding (Lifshitz, 1963; Raj & Ashby, 1971; Langdon, 1975). Experimental observations of fine-grained samples deformed to large strain have led to a description of grain switching events in which trajectories of grain centers are not parallel but rather perpendicular to each other as the central microstructural and topological characteristic (Ashby & Verrall, 1973). Deformation is often referred to as superplastic in this domain, but we will reserve that terminology for large strain deformation experiments and refer to the deformation process described here as grain boundary sliding accommodated by diffusional or dislocation processes (Hirth & Kohlstedt, 1995*a*, 1995*b*).

If melt is present, equation (1) must be modified. Based on an analysis of published creep data, Kelemen *et al.* (1997) observed that an exponential relation could approximate the increase of strain rate with increasing melt fraction such that the creep equation can be written in the form

$$\begin{aligned}\dot{\varepsilon}_\varphi &= \dot{\varepsilon}_{\varphi=0}\exp[\alpha\varphi(T)] \\ &= \dot{\varepsilon}_0\left(\frac{\sigma}{\mu}\right)^n\left(\frac{b}{d}\right)^p f_{O_2}^m(T)a_{SiO_2}^q(T) \\ &\quad\times\exp[\alpha\varphi(T)]\exp\left(-\frac{Q_{ss}}{RT}\right)\end{aligned} \tag{2}$$

where the value of α may depend on the deformation mechanism [see also Mei *et al.* (2002)]. Q_{ss}, the subsolidus activation energy for creep, is the appropriate activation energy provided that a change in creep mechanism does not occur in crossing the solidus temperature. If the flow law is written in the form of equation (2), then the total derivative of the strain rate with respect to temperature can be written as

$$\begin{aligned}\frac{d(\ln\dot{\varepsilon}_\varphi)}{d(1/T)} &= \left[\frac{\partial(\ln\dot{\varepsilon}_\varphi)}{\partial\varphi}\right]_{T,f_{O_2},a_{SiO_2}}\left[\frac{\partial\varphi}{\partial(1/T)}\right]_{f_{O_2},a_{SiO_2}} \\ &\quad+\left[\frac{\partial\dot{\varepsilon}_\varphi)}{\partial(\ln f_{O_2})}\right]_{T,\varphi,a_{SiO_2}}\left[\frac{\partial(\ln f_{O_2})}{\partial(1/T)}\right]_{\varphi,a_{SiO_2}} \\ &\quad+\left[\frac{\partial(\ln\dot{\varepsilon}_\varphi)}{\partial(\ln a_{SiO_2})}\right]_{T,\varphi,f_{O_2}}\left[\frac{\partial(\ln a_{SiO_2})}{\partial(1/T)}\right]_{\varphi,f_{O_2}} \\ &\quad+\left[\frac{\partial(\ln\dot{\varepsilon}_\varphi)}{\partial(1/T)}\right]_{\varphi,f_{O_2},a_{SiO_2}}\end{aligned} \tag{3}$$

that is,

$$\frac{d(\ln\dot{\varepsilon}_\varphi)}{d(1/T)} \equiv -\frac{Q_{hs}^*}{R} = \alpha\left[\frac{\partial\varphi}{\partial(1/T)}\right]_{f_{O_2},a_{SiO_2}} - \frac{Q_{ss}^*}{R} \tag{4a}$$

with

$$\frac{Q_{ss}^*}{R} = m\left[\frac{\partial(\ln f_{O_2})}{\partial(1/T)}\right]_{\varphi,a_{SiO_2}} + q\left[\frac{\partial(\ln a_{SiO_2})}{\partial(1/T)}\right]_{\varphi,f_{O_2}} - \frac{Q_{ss}}{R} \tag{4b}$$

where Q_{hs}^* and Q_{ss}^* are the apparent hypersolidus and subsolidus activation energies, respectively. The oxygen fugacity exponent m in the first term on the right-hand side (RHS) of equation (4b) will be discussed briefly below in light of existing experimental results. Values for the constant α and the subsolidus activation energy Q_{ss} will be presented with the results of our temperature stepping experiments.

EXPERIMENTAL DETAILS

Starting material and sample preparation

We prepared high-density samples by hot-pressing ground powders of spinel lherzolite, derived from a mantle xenolith from Damaping in the Hubei Province of Eastern China. The bulk mineral composition of this spinel lherzolite is 62 vol. % olivine, 26 vol. % orthopyroxene, 10 vol. % clinopyroxene, and 2 vol. % spinel. We separated powders into particle size ranges of 0–10, 10–25 and 25–45 μm to prepare samples used to determine the grain-size dependence of creep rate. The original distribution of mineral phases was maintained in each particle size range within ±3 vol. %. Small grain sizes enhance deformation kinetics, eliminate microcracking, and promote attainment of equilibrium melt distributions during hot-pressing above the solidus temperature. We dried the powders for at least 12 h in a controlled-atmosphere furnace using a mixture of CO–CO_2 gases to maintain an oxygen fugacity corresponding to the Ni–NiO reaction at 1173–1323 K. Dried powders were stored at 413 K in a vacuum drying oven until we uniaxially cold-pressed individual powder fractions into Ni cans at a pressure of 250 MPa. Cold-pressed samples were then returned to the vacuum drying oven for at least 12 h prior to hot-pressing. The Ni cold-press cans were closed on both ends by Ni caps and enclosed in an Fe (low-carbon steel) tube into which ceramic and hardened steel pistons were enclosed as part of the hot-press and deformation assemblies. Samples were hot-pressed at 1373, 1473 or 1523 ± 5 K and 300 MPa for 3–8 h in an internally heated gas-medium pressure vessel.

The oxygen fugacity during hot-pressing and deformation was buffered near Ni–NiO by oxidation of the nickel can, as evidenced by the presence of a NiO layer on the outside of the samples after hot-pressing and deformation and by the lack of metallic nickel in the samples. Samples were end-loaded with a force of a few kilonewtons during hot-pressing to monitor compaction of the sample. All hot-pressed samples had <2 vol. % porosity as determined by optical microscopy.

After hot-pressing, the iron jacket and nickel can were dissolved in a 50/50 mixture of hydrochloric and nitric acids. A 1 mm thick slice from one end of the hot-pressed sample was retained for determining the starting grain size distribution, water content and melt topology. Comparison of slices taken from different locations in several hot-pressed samples using scanning electron microscopy (SEM) and optical microscopy revealed no difference in grain size or melt distribution. This situation does not apply for deformed samples, however, which are subject to spatial variations in stress state as a result of friction at the ends of the sample. We prepared the hot-pressed cylinders for deformation as follows: (1) the ends of the sample were ground square and parallel, to maintain alignment of the deformation column during our experiments; (2) samples were rinsed in acetone, ethanol and deionized water to remove any residual oil or acid; (3a) the hot-pressed samples were stored in the vacuum drying oven at 413 K for at least 12 h prior to deformation; (3b) some hot-pressed samples were dried further in a 1 atm furnace by heating and cooling slowly to and from 1273 K over a period of about 24 h using a $CO–CO_2$ mixture to maintain the f_{O_2} in the olivine stability field. The water content of the samples was measured before and after deformation using Fourier transform infrared (FTIR) spectroscopy with an IR microscope with 10 μm lateral resolution using polished thin sections. Infrared spectra were converted to water concentration by using the calibration described by Paterson (1982); recent calibrations indicate that this approach underestimates the water content in olivine by a factor of ~3·5 (Bell *et al.*, 2003; Koga *et al.*, 2003). A detailed description of the IR analysis technique has been given by Kohlstedt *et al.* (1996). The melt fraction φ was determined using both SEM and optical microscopy. The solidus temperature $T_s \approx 1433$ K was determined for each grain size range from a series of samples hot-pressed and quenched at 10 K increments between 1373 K and 1473 K (see Appendix B for melt fraction data). The solidus was also readily discernible during temperature stepping experiments from the apparent change in activation energy. The olivine, orthopyroxene and clinopyroxene in the starting material are all stable under the temperature and pressure conditions of our experiments based on X-ray diffraction patterns of the starting material and deformed samples.

Deformation experiments

We performed triaxial compression experiments in an internally heated argon-medium pressure apparatus similar to that described in detail by Paterson (1990). Temperature was monitored and controlled to approximately ±2 K over the length of the sample, and the internal load was controlled to within 100 N corresponding to a differential stress of approximately ±1 MPa. The deformation sample assembly and basic procedures are the same as those reported by Hirth & Kohlstedt (1995*a*). We conducted experiments at temperatures from 1373 to 1573 K, confining pressure of 300 MPa, and differential stresses from 5 to 380 MPa. Generally, constant load creep tests were performed on individual samples at several loads at constant temperature to determine the stress exponent, or at several temperatures at approximately the same stress to determine the activation energy for creep. Creep tests were often preceded by constant displacement rate tests to estimate the strength of the sample without exceeding the fracture strength of the sample. We also carried out several constant displacement rate tests to strains of $>30\%$ for comparison with experiments performed in other laboratories and to confirm that creep tests to $<1\%$ axial strain had reached steady state. Differential stress was calculated from the measured load, taking into account the increase in cross-sectional area of the sample with increasing strain, assuming constant volume deformation of a right circular cylinder. Values of stress were also corrected for the load supported by the iron jacket and nickel sleeve as well as for apparatus distortion during constant displacement rate experiments.

Microstructural observations were made using both optical microscopy and SEM. Initial and final grain size distributions were determined from measurements of over 250 grains from both reflected and transmitted light images using the mean linear intercept method with a correction factor of 1·5 (Gifkins, 1970). Melt fractions were determined primarily from binary images of optical micrographs and verified with SEM images as well.

Initial microstructure

After hot-pressing, mean sample grain sizes ranged from 5 to 20 μm as summarized in Table 1. The initial microstructures of two samples after the hot-press are recorded in the transmitted and reflected light images in Fig. 1a and b. Grain size distribution for the hot-pressed sample shown in the top transmitted light micrograph (Fig. 1a) is presented in Fig. 1c as

Table 1: Experimental results for deformation of lherzolite

Exp. no.	T (K)	φ	d_t (μm)	d^* (μm)	σ (MPa)	$\dot{\varepsilon}$ (s^{-1})	d_i (μm)	d_f (μm)	% strain	Total %
42	1473	0·03	16·0	14·3	†	†	15·7	17	5·3	14
			16·1		127	$1·5 \times 10^{-5}$			2·0	
			16·3		78	$4·4 \times 10^{-6}$			1·6	
			16·6		44	$1·7 \times 10^{-6}$			1·1	
			16·8		105	$5·5 \times 10^{-6}$			1·1	
			16·9	17·6	160	$1·2 \times 10^{-5}$			2·2	
			17·0		82	$3·3 \times 10^{-6}$			0·7	
45	1473	0·03	9·3	14·7	†	†	8·4	11	7·9	19
			9·5		133	$2·3 \times 10^{-5}$			4·0	
			9·9		57	$9·0 \times 10^{-6}$			1·8	
			10·4		27	$4·0 \times 10^{-6}$			1·5	
			10·7		104	$1·6 \times 10^{-5}$			2·9	
			11·0		35	$4·3 \times 10^{-6}$			0·7	
46	1473	0·03	5·6		†	†	5	10	3·3	26
			6·7		34	$1·3 \times 10^{-5}$			5·3	
			7·9		15	$5·3 \times 10^{-6}$			2·7	
			8·7		25	$9·1 \times 10^{-6}$			4·2	
			9·2		46	$1·5 \times 10^{-5}$			4·4	
			9·7		59	$1·7 \times 10^{-5}$			5·5	
			10·0		25	$7·0 \times 10^{-6}$			0·6	
48	1473	0·03	10·0	18·6	†	†	9·5	12	6·6	17
			10·5		82	$9·4 \times 10^{-6}$			4·4	
			10·9		35	$4·1 \times 10^{-6}$			1·8	
			11·4		16	$1·9 \times 10^{-6}$			0·8	
			11·7		70	$7·0 \times 10^{-6}$			2·1	
			11·9		100	$1·0 \times 10^{-5}$			1·4	
			12·0		43	$6·0 \times 10^{-6}$			0·2	
71‡	1473	0·03	5·6		10	$2·2 \times 10^{-6}$	5	10·7	1·7	25
			7·9		†	†			3·5	
			8·6		31	$1·1 \times 10^{-5}$			3·9	
			9·1		10	$2·6 \times 10^{-6}$			0·8	
			9·6		22	$6·3 \times 10^{-6}$			2·1	
			10·0		43	$1·3 \times 10^{-5}$			2·8	
			10·1		76	$2·7 \times 10^{-5}$			2·8	
			10·3		88	$3·2 \times 10^{-5}$			2·2	
			10·5		†	†			0·2	
			10·7		94	$3·3 \times 10^{-5}$			5·0	
76	1473	0·03	16·1		55	$3·0 \times 10^{-6}$	16	17	0·6	15
			16·2		71	$4·1 \times 10^{-6}$			0·6	
			16·3		89	$5·5 \times 10^{-6}$			0·6	
			16·5		33	$1·3 \times 10^{-6}$			0·6	
			16·6		54	$2·0 \times 10^{-6}$			0·4	
			16·7	30·0	107	$6·2 \times 10^{-6}$			0·8	
			16·7	21·6	137	$1·0 \times 10^{-5}$			0·9	
			16·8	16·1	171	$2·0 \times 10^{-5}$			1·8	
			16·8	13·3	198	$3·0 \times 10^{-5}$			2·7	
			16·9	10·8	231	$4·9 \times 10^{-5}$			2·3	

Table 1: continued

Exp. no.	T (K)	φ	d_t (μm)	d^* (μm)	σ (MPa)	$\dot{\varepsilon}$ (s^{-1})	d_i (μm)	d_f (μm)	% strain	Total %
			16·9	27·8	113	$1·2 \times 10^{-5}$			1·1	
			17·0	9·9	247	$1·1 \times 10^{-4}$			2·4	
			17·0	16·4	168	$3·4 \times 10^{-5}$			0·5	
84†	1473	0·03	16·1	9·0	264	$5·2 \times 10^{-5}$	16	17	4·9	9
			16·2		65	$2·4 \times 10^{-6}$			0·5	
			16·4		96	$2·1 \times 10^{-6}$			0·9	
			16·6	24·4	125	$2·2 \times 10^{-6}$			0·8	
			16·8	18·6	154	$2·0 \times 10^{-6}$			0·6	
			16·9	12·1	212	$3·7 \times 10^{-6}$			0·8	
			16·9	8·7	271	$6·1 \times 10^{-6}$			0·7	
			17·0	15·2	178	$2·1 \times 10^{-6}$			0·2	
118§	1373	0	16·2		40	$9·7 \times 10^{-8}$	16	17	0·1	7
			16·3	11·2	225	$1·1 \times 10^{-6}$			0·5	
	1393	0	16·4		39	$3·0 \times 10^{-7}$			0·1	
			16·4	11·3	224	$2·7 \times 10^{-6}$			0·3	
			16·5	11·3	223	$1·4 \times 10^{-6}$			0·8	
	1423	0	16·6		38	$7·3 \times 10^{-7}$			0·2	
			16·6	11·5	220	$4·4 \times 10^{-6}$			0·7	
	1433	<0·01	16·7		37	$7·9 \times 10^{-7}$			0·1	
			16·7	11·6	219	$4·1 \times 10^{-6}$			0·5	
	1443	0·01	16·7		37	$5·6 \times 10^{-7}$			0·1	
			16·8	11·7	217	$5·4 \times 10^{-6}$			0·8	
	1453	0·02	16·8		37	$1·1 \times 10^{-6}$			0·1	
			16·8	11·8	216	$6·4 \times 10^{-6}$			0·7	
	1463	0·03	16·8		37	$9·4 \times 10^{-7}$			0·1	
			16·9	12·0	213	$6·9 \times 10^{-6}$			1·1	
	1473	0·03	16·9		36	$7·3 \times 10^{-7}$			0·1	
			16·9	12·1	211	$7·7 \times 10^{-6}$			1·0	
	1453	0·02	17·0	12·2	210	$4·0 \times 10^{-6}$			0·4	
	1433	<0·01	17·0	12·3	209	$1·1 \times 10^{-6}$			0·1	
129	1423	0	19·1	18·8	152	$8·7 \times 10^{-7}$	19	19·5	0·2	2
			19·1	33·6	98	$2·0 \times 10^{-7}$			0·1	
	1433	<0·01	19·2	20·0	145	$1·3 \times 10^{-6}$			0·2	
			19·2	17·9	158	$1·3 \times 10^{-6}$			0·2	
			19·3	33·9	98	$3·5 \times 10^{-7}$			0·1	
	1443	0·01	19·3	32·0	102	$1·1 \times 10^{-6}$			0·2	
			19·4	17·6	160	$1·8 \times 10^{-6}$			0·4	
	1453	0·02	19·4	33·5	99	$1·2 \times 10^{-6}$			0·2	
	1463	0·03	19·5	33·9	98	$1·5 \times 10^{-6}$			0·4	
	1473	0·03	19·5	34·2	97	$2·3 \times 10^{-6}$			0·5	
131§	1373	0	14·6		42	$9·2 \times 10^{-7}$	14·6	15	0·5	16
			14·7	11·4	221	$3·5 \times 10^{-6}$			0·9	
	1393	0	14·7		44	$1·1 \times 10^{-6}$			0·6	
			14·7	11·0	227	$3·7 \times 10^{-6}$			1·7	
	1413	0	14·8		42	$1·1 \times 10^{-6}$			0·7	
			14·8	10·9	229	$4·2 \times 10^{-6}$			1·1	
	1433	<0·01	14·8		40	$7·6 \times 10^{-7}$			0·5	
			14·8	11·0	227	$4·9 \times 10^{-6}$			0·9	

Exp. no.	T (K)	φ	d_t (μm)	d^* (μm)	σ (MPa)	$\dot{\varepsilon}$ (s^{-1})	d_i (μm)	d_f (μm)	% strain	Total %
	1443	0·01	14·9		41	$4·7 \times 10^{-7}$			0·3	
			14·9	11·0	228	$6·1 \times 10^{-6}$			1·2	
	1453	0·02	14·9		40	$6·5 \times 10^{-7}$			0·3	
			14·9	11·0	227	$9·9 \times 10^{-6}$			1·0	
	1463	0·03	14·9		40	$1·2 \times 10^{-6}$			0·3	
			15·0	11·0	228	$1·4 \times 10^{-5}$			1·2	
	1473	0·03	15·0		41	$2·1 \times 10^{-6}$			0·3	
			15·0	11·1	225	$2·1 \times 10^{-5}$			1·2	
	1493	0·04	15·0		42	$4·2 \times 10^{-6}$			0·5	
			15·0	11·2	224	$5·0 \times 10^{-5}$			1·1	
	1513	0·05	15·0		46	$9·0 \times 10^{-6}$			1·2	
137§	1373	0	20·9		38	$9·7 \times 10^{-8}$	20·9	21	0·1	3
	1393	0	20·9		39	$6·4 \times 10^{-8}$			0·03	
	1413	0	20·9		39	$9·8 \times 10^{-8}$			0·1	
	1433	<0·01	20·9		40	$2·6 \times 10^{-7}$			0·1	
	1443	0·01	21·0		40	$2·9 \times 10^{-7}$			0·1	
	1453	0·02	21·0		41	$3·6 \times 10^{-7}$			0·2	
	1463	0·03	21·0		41	$6·1 \times 10^{-7}$			0·2	
	1473	0·03	21·0		43	$7·5 \times 10^{-7}$			0·3	
	1493	0·04	21·0		42	$1·4 \times 10^{-6}$			0·3	
	1523	0·05	21·0		44	$6·0 \times 10^{-6}$			0·9	
	1433	<0·01	21·0		45	$4·5 \times 10^{-7}$			0·1	
	1443	0·01	21·0		45	$4·3 \times 10^{-7}$			0·1	
	1413	0	21·0		45	$3·1 \times 10^{-7}$			0·03	
163§	1373	0	16·2	11·2	224	$2·1 \times 10^{-6}$	16	17	1·6	13
	1393	0	16·5	11·3	223	$3·0 \times 10^{-6}$			2·3	
	1413	0	16·7	11·3	223	$4·3 \times 10^{-6}$			2·2	
	1433	<0·01	16·8	11·3	223	$5·7 \times 10^{-6}$			2·6	
	1453	0·02	16·9	11·4	221	$8·5 \times 10^{-6}$			2·0	
	1473	0·03	17·0	11·4	222	$1·5 \times 10^{-5}$			2·6	
164	1473	0·03	17·1	11·5	219	$1·3 \times 10^{-5}$	17	17·5	3·8	14
	1493	0·04	17·2	12·0	214	$3·0 \times 10^{-5}$			3·6	
	1513	0·05	17·3	12·4	208	$6·5 \times 10^{-5}$			5·6	
	1433	<0·01	17·5	11·3	223	$2·3 \times 10^{-6}$			0·9	
165‡	1373	0	16·3		42	$1·1 \times 10^{-7}$	16	17	0·01	2
			16·3	11·2	†‡	†‡			0·1	
	1393	0	16·5		45	$1·9 \times 10^{-7}$			0·01	
			16·5	9·9	245	$1·3 \times 10^{-6}$			0·3	
	1413	0	16·7		55	$3·3 \times 10^{-7}$			0·1	
			16·8	10·5	235	$2·1 \times 10^{-6}$			0·7	
	1433	<0·01	16·9		61	$5·6 \times 10^{-7}$			0·03	
			17·0	10·2	241	$3·5 \times 10^{-6}$			0·8	
166	1373	0	17·3		64	$2·0 \times 10^{-7}$	17	18	0·01	7
			17·4	10·2	240	$3·3 \times 10^{-7}$			0·1	
	1413	0	17·5		74	$5·5 \times 10^{-7}$			0·1	
			17·6	9·6	252	$1·4 \times 10^{-6}$			0·5	
	1453	0·02	17·8		80	$1·0 \times 10^{-6}$			0·5	
			17·8	9·5	255	$5·5 \times 10^{-6}$			1·5	
	1473	0·03	18·0		87	$3·4 \times 10^{-6}$			1·1	
			18·0	9·6	252	$2·8 \times 10^{-5}$			3·2	

Table 1: continued

Exp. no.	T (K)	φ	d_t (μm)	d^* (μm)	σ (MPa)	$\dot{\varepsilon}$ (s^{-1})	d_i (μm)	d_f (μm)	% strain	Total %
177	1373	0	16·6		†	†	16·5	17	0·01	9
			16·7		68	$1{\cdot}5 \times 10^{-7}$			0·1	
			16·7	10·3	238	$5{\cdot}7 \times 10^{-7}$			0·3	
	1423	0	16·8		62	$5{\cdot}2 \times 10^{-7}$			0·4	
			16·9	10·6	234	$2{\cdot}6 \times 10^{-6}$			1·0	
	1473	0·03	16·9		64	$2{\cdot}9 \times 10^{-6}$			1·1	
			16·9	10·9	229	$9{\cdot}4 \times 10^{-6}$			1·5	
	1523	0·05	17·0		65	$1{\cdot}0 \times 10^{-5}$			1·3	
			17·0	11·3	224	$8{\cdot}8 \times 10^{-5}$			3·1	
			17·0		65	$1{\cdot}3 \times 10^{-5}$			0·4	
215	1473	0·03	9·0		†	†	8	12	0·8	34
			10·3		26	$4{\cdot}0 \times 10^{-6}$			3·4	
			10·8		105	$1{\cdot}8 \times 10^{-5}$			6·2	
			11·0	17·6	160	$3{\cdot}8 \times 10^{-5}$			3·6	
			12·0		119	$2{\cdot}0 \times 10^{-5}$			20·2	
218¶	1498	0·04	17·0	13·3	197	$3{\cdot}7 \times 10^{-5}$	14·5	17	37·9	38
223¶	1523	0·05	16·0		63	$3{\cdot}4 \times 10^{-5}$	5	16	38·5	39
227	1473	0·03	18·3		42	$1{\cdot}2 \times 10^{-6}$	18	19	0·9	8
			18·4	11·1	225	$1{\cdot}3 \times 10^{-5}$			2·8	
	1498	0·04	18·9		42	$2{\cdot}5 \times 10^{-6}$			1·4	
			19·0	11·7	217	$3{\cdot}6 \times 10^{-5}$			3·3	
			19·0		40	$2{\cdot}0 \times 10^{-6}$			0·1	
233	1498	0·04	7·8		†	†	6	14	0·9	21
			9·4		†	†			0·5	
			10·8		35	$5{\cdot}9 \times 10^{-6}$			2·5	
	1523	0·05	12·1		35	$1{\cdot}4 \times 10^{-5}$			3·5	
	1548	0·07	13·1		34	$3{\cdot}4 \times 10^{-5}$			6·0	
	1573	0·09	13·4		33	$6{\cdot}6 \times 10^{-5}$			4·1	
			13·6		15	$2{\cdot}8 \times 10^{-5}$			1·9	
			14·0		†	†			1·4	
239	1473	0·03	12·8		†	†	12·5	14	0·6	15
			13·3		36	$2{\cdot}7 \times 10^{-6}$			1·5	
	1523	0·05	13·7		35	$1{\cdot}8 \times 10^{-5}$			6·4	
	1573	0·09	14·0		36	$8{\cdot}3 \times 10^{-5}$			6·5	
259**	1573	0·1	19·2		33	$5{\cdot}1 \times 10^{-5}$	5	21	7·2	23
			21·0	21·4	138	$6{\cdot}3 \times 10^{-4}$			15·4	

φ is the melt fraction, σ is the applied differential stress, ε is the measured strain rate, d_t is the grain size determined from equation below, d^* is the recrystallized grain size from equation (5.4) of Van der Wal (1993), d_i is the measured average grain size prior to deformation, d_f is the measured average grain size after deformation.

$$d_f^r - d_i^r = kt$$

$$k = k_0(f_{O_2}, a_{SiO_2})\exp(-Q_{gg}/RT)$$

where $r = 3$, $k_0 = 2{\cdot}5 \times 10^5\ m^3/s$, $Q_{gg} = 700\ kJ/mol$.
†Individual strain segment at constant displacement rate. Stress and strain rate are not included here because the sample has not reached steady state during this segment.
‡Zero load reading of internal load cell shifted during deformation.
§FTIR indicated $<30\ H/10^6 Si$.
¶High strain constant displacement rate experiment to steady-state strain rate.
**Excess spinel (Sp) in sample (2 vol. % $<$ [Sp] $<$ 4 vol. %).

a histogram of intercept lengths. Details of the grain size distribution and grain growth in our samples will be presented in a separate paper on grain growth in partially molten lherzolite.

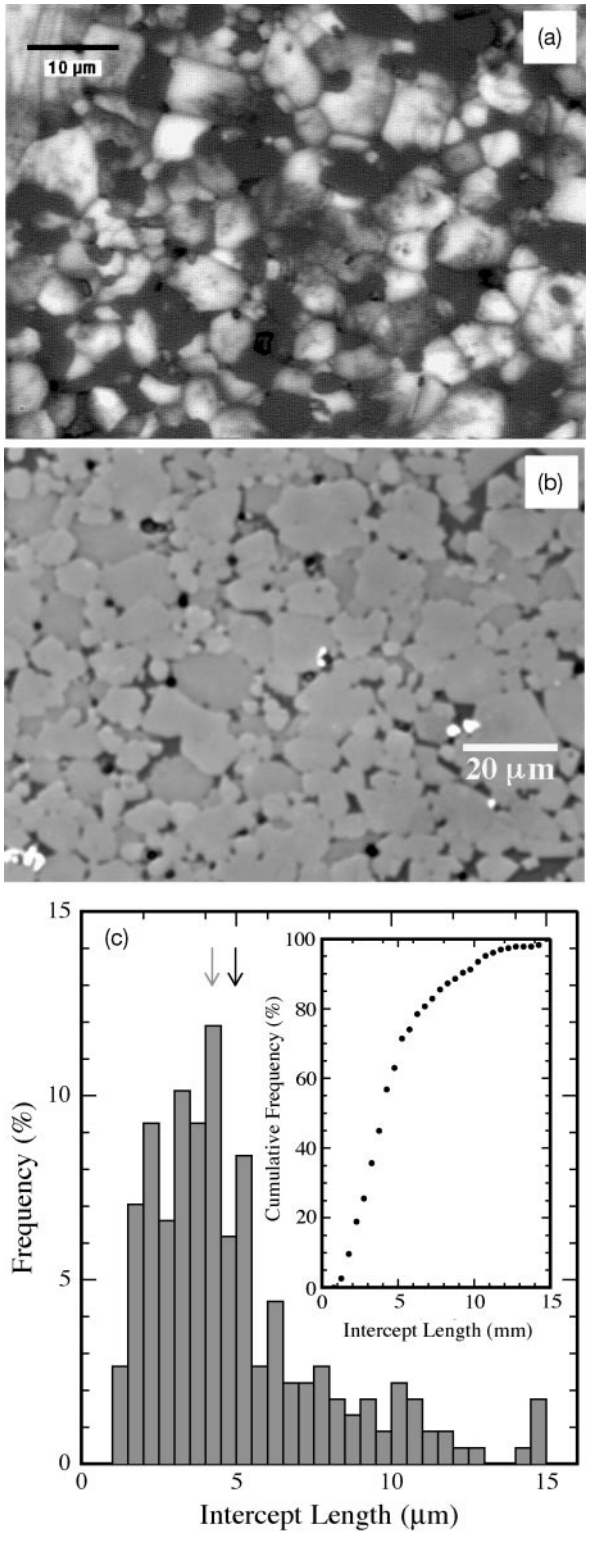

Prior to deformation, the distribution of melt in lherzolite samples hot-pressed above the 1433 K solidus temperature is remarkably similar to that documented for olivine–basalt samples (Waff & Bulau, 1979; Watson, 1982; Cooper & Kohlstedt, 1984; Riley & Kohlstedt, 1991; Beeman & Kohlstedt, 1993; Hirth & Kohlstedt, 1995*a*, 1995*b*). As shown in the micrograph in Fig. 1b, for a sample hot-pressed at 1500 K, the melt phase is present at all triple junctions that include at least one olivine grain and is excluded only from triple junctions surrounded by pyroxene grains. The presence of melt at junctions with at least two olivine grains is consistent with observations for olivine–basalt and partially molten peridotites with pyroxene (Cooper & Kohlstedt, 1984; Riley & Kohlstedt, 1991; Beeman & Kohlstedt, 1993; Hirth & Kohlstedt, 1995*a*, 1995*b*). Initial melting occurs at contacts where all four solid phases are present. Thus, the presence of melt at boundaries with olivine as the only solid phase, even at low melt fractions, indicates that the melt phase is able to redistribute during a 3 h hot-press. The influence of anisotropic surface energy is also evident in the hot-pressed lherzolite samples as indicated by the presence of relatively thick ($\sim$1 μm) films of melt along some but not all of the grain boundaries (Hiraga *et al.*, 2002). The anisotropic distribution of melt along grain boundaries is well documented for olivine–basalt aggregates (e.g. Cooper & Kohlstedt, 1984; Waff & Faul, 1992; Faul *et al.*, 1994).

Lherzolite samples hot-pressed below the solidus temperature have less equant grain shapes than samples hot-pressed above 1473 K, indicative of lower grain boundary mobility at lower temperatures and therefore less grain growth. However, porosity was still $\sim$2 vol. % in these samples.

Samples dried at 413 K after hot-pressing contained $\leq$30 H/10^{6}Si, whereas samples dried at 1173 to

Fig. 1. (a) Transmitted light micrograph of fine-grained lherzolite sample (46) after hot-press at 1473 K. Scale bar represents 10 μm. Sample contains $\sim$65 vol. % olivine, which is the light gray to white grains in this image. The dark gray and black grains are the ortho- and clinopyroxene grains that constitute $\sim$25 vol. % and $\sim$10 vol. %, respectively. A few small spinel grains $<$2 vol. % are opaque in transmitted light but indistinguishable from the pyroxene grains in this image. The melt phase ($\varphi = 0{\cdot}03$) is also impossible to distinguish in this micrograph. (b) Reflected light micrograph of a lherzolite sample (233) hot-pressed at $\sim$1500 K. Scale bar represents 20 μm. The olivine grains appear slightly lighter gray with darker gray pyroxenes and a few bright white cr-spinel grains. The sample has a melt fraction of $\varphi \approx 0{\cdot}04$, which appears as the darkest gray or black phase distributed in most of the triple junctions and along many grain boundaries, typical of the anisotropic wetting properties of mineral–mineral and mineral–melt interfaces present in hypersolidus lherzolite. (c) Grain size distribution of sample shown in the transmitted light micrograph in (a). Histogram of intercept length vs frequency. Gray arrow (left) and black arrow (right) indicate the median and average intercept lengths, respectively. Inset plot is cumulative frequency vs intercept length for the same sample.

1323 K contained $\leq$10 H/10^{6}Si both before and after deformation.

EXPERIMENTAL RESULTS

The experimental results for lherzolite, summarized in Table 1, are analyzed in relation to the flow law presented in equation (2) to determine the operative creep mechanism(s). Evaluation of our results for lherzolite and the results of Hirth & Kohlstedt (1995*a*, 1995*b*) for olivine and olivine–basalt aggregates reveals that the same deformation mechanisms are operating in both types of samples, with and without melt, and that the magnitude of the strain rate enhancement as a result of the presence of melt is approximately the same. Below, we first consider the creep behavior of melt-free samples as well as the dependence of strain rate on grain size. We then examine the dependence of creep rate of lherzolite on temperature in both the subsolidus and hypersolidus regions, to separate the effects of melt from those of temperature. Finally, we analyze the influence of melt fraction on the deformation of lherzolite for $0{\cdot}0 \leq \varphi \leq 0{\cdot}10$, and we assess the effects of grain size and stress on creep rate in the hypersolidus region to determine if the same processes are controlling the deformation as in the subsolidus temperature range. Only samples with <10 H/10^{6}Si are considered in the subsolidus creep results, to minimize the effect of water on the deformation. Above the solidus temperature, samples with <30 H/10^{6}Si are included in the evaluation because this small amount of water has a minimal effect on creep rate above the solidus temperature (Mei *et al.*, 2002), consistent with the observation that water strongly partitions into the melt (e.g. Michael, 1988). The solidus temperature, $T_s = 1433 \pm 2$ K, was not measurably different between samples with these two water contents.

Although grain growth in our samples occurs predominantly during the initial hot-press stage of sample preparation, continued grain growth does occur during deformation, as shown in Table 1. We compared grain growth in our samples with existing grain growth models to estimate the grain size during each individual creep test (Zimmerman & Kohlstedt, in preparation). Olivine grain growth kinetics were analyzed based on a growth law of the form $d_f^r - d_i^r = kt$, where d_f is the final grain size, d_i is the initial grain size, t is time and k is a rate constant determined for each experiment (e.g. Brook, 1976). A value of $r = 3$ was determined for this study, consistent with an Ostwald ripening process in two-phase solids, in which long-range diffusion controls coarsening kinetics (Fan & Chen, 1997). The grain growth constant has the form $k = k_0 \exp(-Q_{gg}/RT)$, where k_0 is a material parameter and Q_{gg} is the activation energy for grain growth. A reasonable estimate of size of the olivine grains during deformation of lherzolite can be made using $k_0 = 2{\cdot}5 \times 10^5$ m^3/s and $Q_{gg} = 700$ kJ/mol.

Deformation of lherzolite

Our data for subsolidus lherzolite ($T_s = 1433$ K) are limited because of difficulties in preparing well-consolidated fine-grained samples at such low temperatures. We compare our results for subsolidus lherzolite and melt-free olivine in the diffusional creep regime to illustrate that the same mechanisms are operative in these two different materials under similar thermomechanical conditions. However, to confirm that the same mechanisms are operative in both temperature regions, the flow law for lherzolite is ultimately derived in the hypersolidus region and applied to the subsolidus data.

Effect of stress on creep rate at subsolidus temperatures

In Fig. 2, strain rate is plotted as a function of stress for lherzolite samples deformed between 1373 and 1433 K in the diffusional creep regime. The lherzolite samples all had a grain size between 16 and 18 μm. Therefore our data are compared with the results for olivine samples at a grain size of 17 μm and a temperature of 1373 K employing a grain size exponent of $p = 3$ and an activation energy of 375 kJ/mol, the values reported by Hirth & Kohlstedt (2003) and consistent with those obtained in this study. The strain rate of subsolidus lherzolite samples agrees within a factor of two with the flow law for melt-free olivine.

Effect of grain size on creep rate at subsolidus temperatures

Creep results for our subsolidus lherzolite samples and for a melt-free olivine sample from Hirth & Kohlstedt (1995*a*) deformed in the diffusional creep regime are compared on the log–log plot of strain rate vs grain size in Fig. 3. Strain rates are normalized to a stress of 35 MPa using a stress exponent of $n = 1$ and to a common temperature of 1373 K using an activation energy of 375 kJ/mol. Based on grain sizes measured before and after deformation, the grain size for individual creep tests was determined using the grain growth law presented above. A linear least-squares fit of the lherzolite data closely parallels the flow law for melt-free olivine (Hirth & Kohlstedt, 2003), indicating that the deformation mechanism is the same in both cases with a grain size exponent of $p = 3$ and a stress exponent of $n = 1$, characteristic of creep rate-limited by grain boundary diffusion (Coble, 1963; Raj & Ashby, 1971).

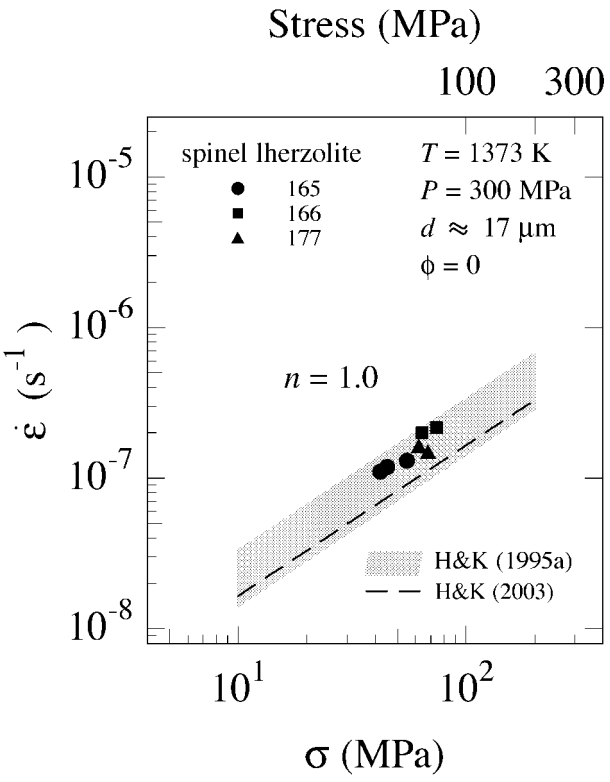

Fig. 2. Strain rate vs differential stress for three samples of lherzolite deformed at 1373 K and three samples of nominally melt-free olivine. The latter define the gray shaded area. Olivine data from Hirth & Kohlstedt (1995*a*) are normalized to 1373 K using $Q = 375$ kJ/mol (Hirth & Kohlstedt, 2003) and to a grain size of 17 μm assuming $n = 1$ and $p = 3$ in equation (1). The dashed line is the flow law from the review paper by Hirth & Kohlstedt (2003). The similarity of the data for lherzolite and for olivine indicates that deformation occurs by diffusional creep in both types of samples.

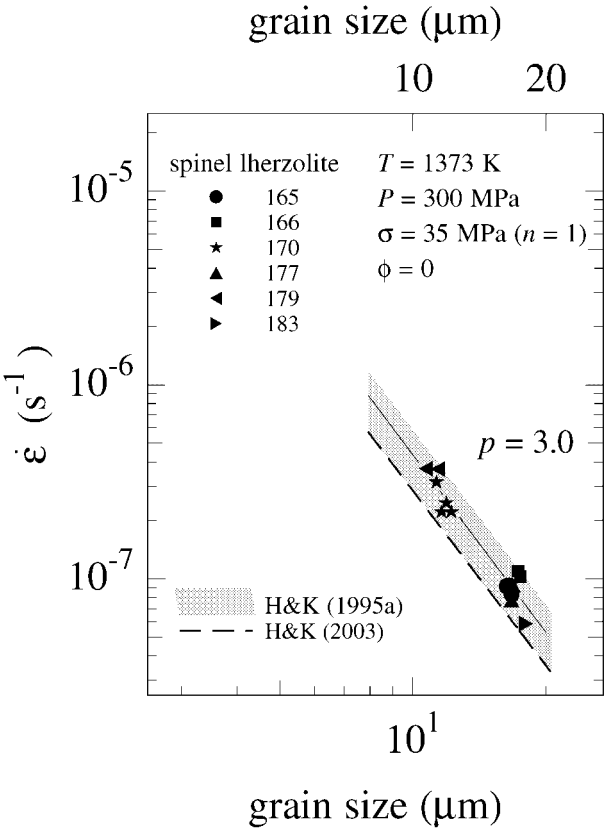

Fig. 3. Plot of strain rate vs grain size for six samples of lherzolite deformed at 1373 K and one sample of nominally melt-free olivine. The latter defines the gray shaded area. Olivine results from Hirth & Kohlstedt (1995*a*) are normalized to 1373 K using $Q = 375$ kJ/mol. The dashed line is the Hirth & Kohlstedt (2003) flow law. The value of the grain size exponent of $p = 3$ indicates that deformation occurred by grain boundary diffusion.

Effect of grain size on creep rate at hypersolidus temperatures

The dependence of creep rate on grain size in the diffusional creep regime, expressed as the grain size exponent p in equation (1), is determined in Fig. 4 for lherzolite at 1473 K with a melt fraction of $\varphi \approx 0{\cdot}03$ from a linear least-squares fit to the strain rate vs grain size data on this log–log plot. Data are reported for nine lherzolite samples deformed at $\sigma \leq 50$ MPa, as the dislocation contribution to the creep rate is $<10\%$ (see Appendix A). Strain rates are normalized to a common value of $\sigma = 35$ MPa using $n = 1$. The grain size exponent of $p = 3{\cdot}0 \pm 0{\cdot}5$ determined from the fit is the same as the grain size exponent obtained for subsolidus lherzolite in conjunction with the melt-free olivine data, and is indicative of diffusional creep controlled by grain boundary diffusion (Coble, 1963). The melt-added olivine sample of Hirth & Kohlstedt (1995*a*), indicated by the gray band in Fig. 4, had a melt fraction of $\varphi \approx 0{\cdot}02$ and was deformed at 1523 K. Consequently, the corresponding strain rates have been normalized to a common temperature using $Q_{\varphi=0} = 375$ kJ/mol and to a common melt fraction using $\alpha = 30$ (Hirth & Kohlstedt, 2003).

Effect of stress on creep rate at hypersolidus temperatures

The transition from diffusional creep with $n \approx 1$ to dislocation creep with $n \approx 3$ to 5 as reported for melt-free olivine also occurs during creep of lherzolite samples. This point is illustrated in Fig. 5, a plot of strain rate vs stress for lherzolite samples deformed at 1473 K with a melt fraction of $\varphi = 0{\cdot}03$, normalized to a common grain size of $d = 17$ μm. A non-linear least-squares fitting algorithm was used to fit the data to the constitutive equation

$$\dot{\varepsilon}_\varphi = A_1(T, P, d, \varphi) \times \sigma^{n_1} + A_2(T, P, \varphi) \times \sigma^{n_2} \quad (5)$$

formed assuming that diffusional creep (mechanism 1) and dislocation creep (mechanism 2) are independent

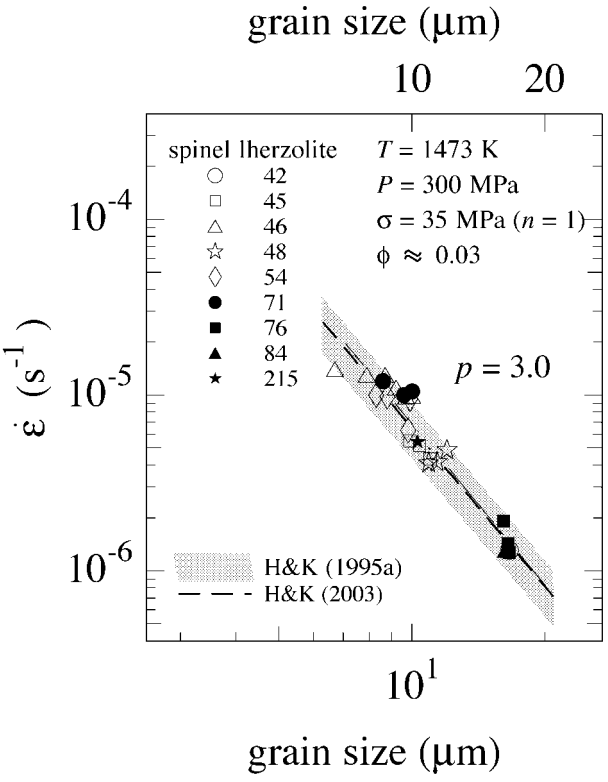

Fig. 4. Strain rate vs grain size for our partially molten lherzolite samples with $\varphi \approx 0{\cdot}03$ and an olivine plus basalt sample with $\varphi \approx 0{\cdot}02$ from Hirth & Kohlstedt (1995*a*). Experiment run numbers are indicated next to the corresponding symbol. The lherzolite samples were deformed at $T = 1473$ K, $P = 300$ MPa and differential stresses of <100 MPa. Data are normalized to a stress of 35 MPa using $n = 1$. The data from an olivine sample deformed at 1523 K were normalized using $Q_{HK} = 375$ kJ/mol (gray-shaded region). Sample numbers are indicated next to the corresponding symbols. The slope of $p = 3$ from equation (2) indicates that the deformation is controlled by grain boundary diffusion.

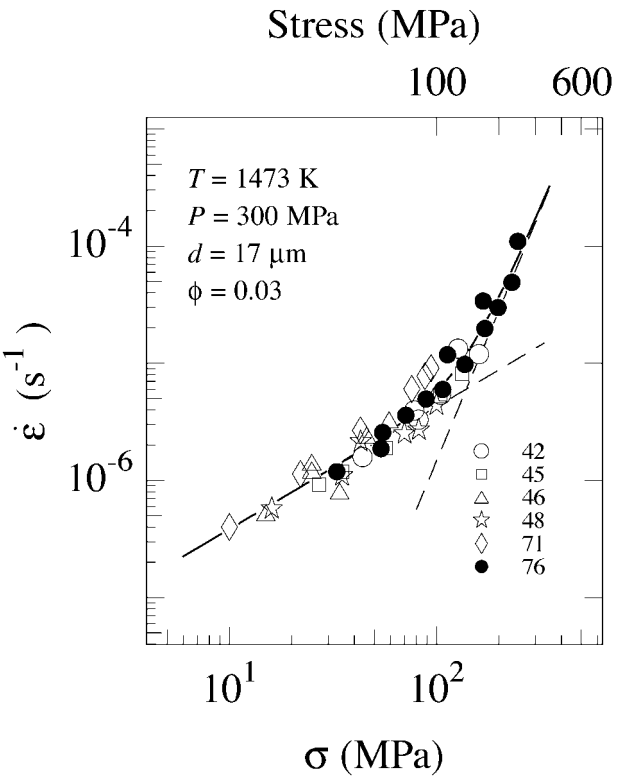

Fig. 5. Strain rate vs differential stress for six lherzolite samples deformed at $T = 1473$ K and $P = 300$ MPa with a melt fraction of $\varphi = 0{\cdot}03$, normalized to a common grain size of $d = 17$ μm. The data are fitted using a non-linear least-squares fitting technique as indicated by the continuous curved line and explained in the text. A transition from diffusional creep to dislocation creep occurs at $\sigma \approx 140$ MPa as indicated by the two dashed lines, one with $n = 1$ at low stress and the other with $n = 4{\cdot}3$ at higher stresses.

(parallel) processes, each described by a flow law of the type given in equation (2) (e.g. Parrish & Gangi, 1981). In equation (5), A_1, n_1, A_2 and n_2 are varied to minimize the least-squares deviation of the data from the function. The parameters A_1 and A_2 are constant for a given T, P, d and φ. In Fig. 5 the constitutive equation (continuous line) as well as the diffusional and dislocation flow laws (dashed lines) are shown. The transition from diffusional creep to dislocation creep occurs at $\sigma \approx 140$ MPa for this grain size. It should be noted that the constitutive equation reaches 90% of the diffusional creep flow law at $\sigma \approx 60$ MPa and 90% of the dislocation creep flow law at $\sigma \approx 240$ MPa (see Appendix A).

Effect of temperature and melt fraction on creep rate

The dependence of strain rate on temperature and melt fraction (i.e. Q_{ss} and α)for diffusional and dislocation creep of lherzolite were determined from creep data obtained at temperatures in the range 1373–1573 K. Because melt fraction changes with temperature in lherzolite samples, it was necessary to determine the dependence of melt fraction on temperature as presented in Appendix B. Below we treat first the diffusional creep regime and then the dislocation creep regime. The subsolidus activation energy Q_{ss} becomes Q_{diff} and Q_{disl}, the activation energies for diffusional and dislocation creep, respectively.

To determine the activation parameters in the diffusional creep regime and include a larger range of strain rates, we selected data that are ≥90% diffusional as determined from Fig. 5 (and Fig. A1 in Appendix A) and fit the data to a diffusional creep equation of the form of equation (1) with $n = 1$ and $p = 3$ under the assumption that creep rate is independent of oxygen fugacity and silica activity. The resulting values, shown in Fig. 6a, for Q_{diff} and α_{diff} are 370 ± 30 kJ/mol and 21 ± 3, respectively.

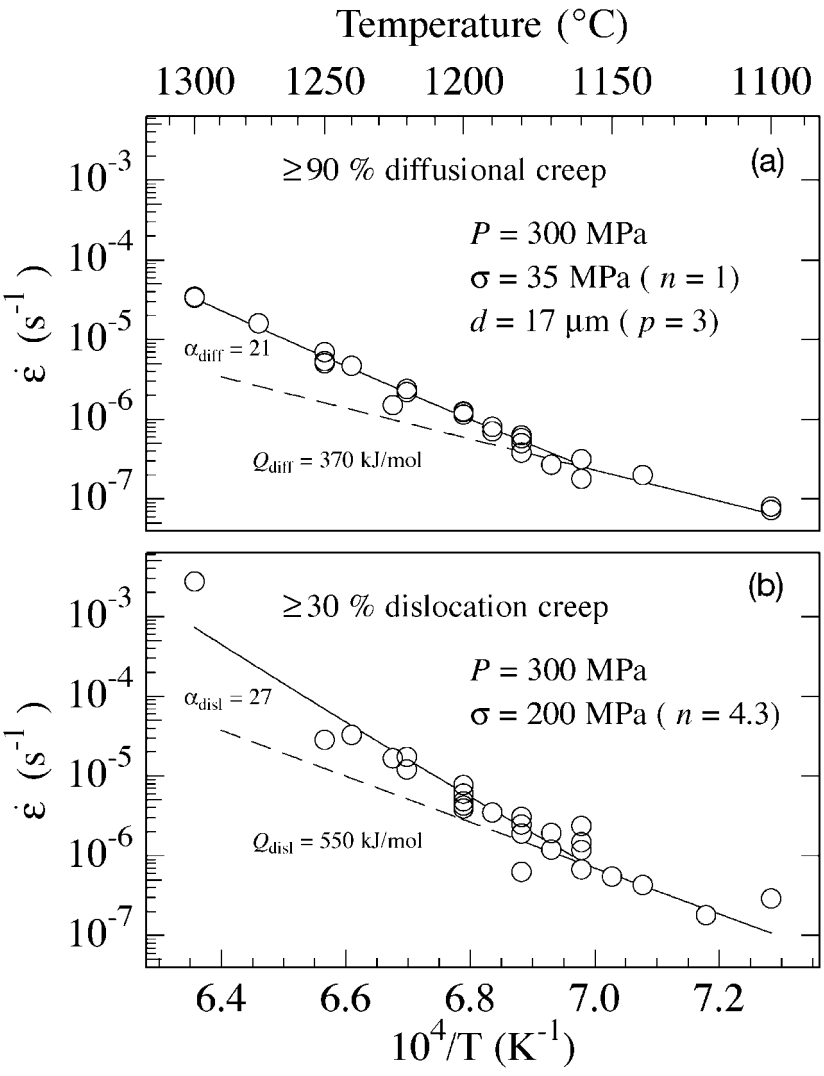

Fig. 6. Arrhenius plots of strain rate vs temperature for 11 samples of lherzolite. Samples contained <30 H/10^6Si before and after deformation as determined by FTIR. (a) Samples deformed in the diffusional creep regime normalized to a differential stress of 35 MPa using $n = 1$ and to a common grain size of 17 μm using $p = 3$ in equation (1). An activation energy of $Q_{diff} = 370$ kJ/mol and a value of $\alpha_{diff} = 21$ were determined from a non-linear least-squares fit to the data. (b) Samples deformed in the dislocation creep regime are normalized to a differential stress of 200 MPa using $n = 4{\cdot}3$ in equation (1). An activation energy of $Q_{disl} = 550$ kJ/mol and a value of $\alpha_{disl} = 27$ were determined from a non-linear least-squares fit to the data (see Appendix A).

The selection process is more complicated in the dislocation regime because of the limited amount of data obtained during temperature stepping experiments above 240 MPa (the stress level for which dislocation creep contributes ≥90% to the total strain rate as determined from Fig. 5 and Fig. A1 in Appendix A). Consequently, we have selected creep rates to include data with ≥30% dislocation creep contribution. The diffusional creep portion of the strain rate is then subtracted from the total strain rate; the remaining strain rates are normalized to a stress of 200 MPa and fitted to a dislocation creep equation of the form of equation (1) with $n = 4{\cdot}3$, as illustrated in Fig. 6b. The values determined for Q_{disl} and α_{disl} are 550 ± 50 kJ/mol and 27 ± 5, respectively. [Activation energies reported in this study are apparent activation energies for creep because they include not only the dependence of creep rate on temperature but also the dependence of creep rate on oxygen fugacity, which is a function of temperature for a metal–metal-oxide buffer. Previous studies on single crystal and polycrystalline olivine samples reported a range of values for the oxygen fugacity exponent m from 0 to 1/3 (Bai *et al.*, 1991; Beeman & Kohlstedt, 1993; Hirth & Kohlstedt, 1995*a*). Based on equation (1), this range would result in a reduction in our apparent activation energies by

Table 2: Flow law parameters for lherzolite in equation (2)

Creep regime	$\dot{\varepsilon}_0^*$	p	n	α	Q_{ss} (kJ/mol)
Diffusional	$8{\cdot}54 \times 10^{23}$	3	1	21	370
Dislocation	$2{\cdot}64 \times 10^{25}$		4·3	27	550

*The pre-exponential term has been normalized by the shear modulus, μ (61 GPa) for olivine at 1473 K (Webb, 1989) and the length of the Burgers vector, b (0·475 nm) for the [100] (Deer *et al.*, 1992) ($A_{diff} = 1{\cdot}5 \times 10^9$, $A_{disl} = 7{\cdot}0 \times 10^4$).

0–160 kJ/mol for olivine samples buffered at a constant oxygen fugacity rather than with a fixed oxide buffer (i.e. Ni–NiO). Additional experiments under controlled oxygen fugacity conditions are required to constrain the magnitude of this effect on the creep of lherzolite.] If the data selected have a contribution of $>50\%$ dislocation creep, the value of Q_{disl} does not change and the value of α_{disl} changes only slightly to 26, well within experimental error for these samples. The values of A, n, p, α and Q determined from the experimental data for both the diffusional and dislocation creep regimes are reported in Table 2.

As part of this study, two constant displacement rate experiments were also conducted to true strains $>40\%$ to compare the flow behavior with previous studies that reported dramatic strain weakening in partially molten peridotite samples after $\sim$10% strain (Jin *et al.*, 1994). As illustrated in Fig. 7 for one of the constant displacement rate experiments for a sample with $\varphi \approx 0{\cdot}05$, no stress drop occurred in these samples. It should be noted that we also do not observe a progressive weakening of the sample with strain that might be associated with realignment of melt-bearing grain boundaries subparallel to σ_1. For comparison, the results from a constant load experiment on a sample with $\varphi \approx 0{\cdot}03$ deformed to a true strain of >30% are included in Fig. 7. The inserted plot in Fig. 7 demonstrates that steady-state conditions are reached by a strain of $\approx 0{\cdot}5\%$ in the constant load experiments, whereas attainment of steady state requires a strain of >10% in constant displacement rate experiments. Shear experiments performed in our laboratory on lherzolite samples to a shear strain of >200% yield results consistent with the compressive creep experiments reported here.

Water content

Fourier transform infrared (FTIR) spectra shown in Fig. 8 indicate that lherzolite samples synthesized from powders that had been pre-dried in a 1 atm furnace contained only a small amount of water before and after deformation. Samples stored in a vacuum drying oven after the hot-press contained $<30\,H/10^6Si$, whereas samples reheated to $T = 1273$ K after the hot-press contained $<10\,H/10^6Si$, a value near the resolution limit of the IR apparatus. Because of the fine grain size of the lherzolite aggregates, we were unable to determine the distribution of water among grain or phase boundaries, crystals and melt. However, previous work demonstrates that most of the water is in the melt and/or grain or phase boundaries (Mei *et al.*, 2002).

Melt distribution in deformed samples

Microstructures of partially molten lherzolite samples are presented in the reflected light micrographs in Fig. 9a and b. The melt topology is very similar to that in olivine–basalt aggregates, including quenched melt in nearly all three- and four-grain junctions. Melt is present in all these grain junctions that include at least one olivine grain, contrary to previously reported observations of partially molten peridotites (Toramaru & Fujii, 1986). The presence of melt in all of the triple junctions surrounded by olivine grains is a good indication that these fine-grained samples are texturally mature, as melting occurs at junctions with three or more phases present (Waff & Bulau, 1979). At all melt fractions from $\varphi = 0{\cdot}03$ to 0·10, melt is also present along some grain interfaces bordered by one or more faceted grains. The percentage of grain interfaces wetted by melt and the amount of melt along grain boundaries increases continuously with increasing melt fraction as indicated by the continuous increase in strain rate with increasing melt fraction and rising temperature on the Arrhenius plots in Fig. 6a and b. However, we do observe an alignment of melt-filled boundaries 15–20° to the maximum principal stress σ_1 in samples quenched at differential stresses above $\sim$100 MPa. Prominent aligned melt pockets are visible in the optical micrographs of a sample deformed at 1573 K shown in Fig. 9a and b.

DISCUSSION

Diffusional creep

The dependence of creep rate on stress, grain size and temperature observed for lherzolite deformed in the diffusional creep regime in both the subsolidus and hypersolidus regions is similar to the deformation behavior of polycrystalline olivine and olivine–basalt aggregates, as shown in Figs 2, 3 and 4. Deformation is rate limited by grain boundary diffusion as indicated by values of $n = 1$ and $p = 3$ (e.g. Coble, 1963; Hirth & Kohlstedt, 1995*a*). To identify the rate-limiting species, Hirth & Kohlstedt (1995*a*) compared the grain

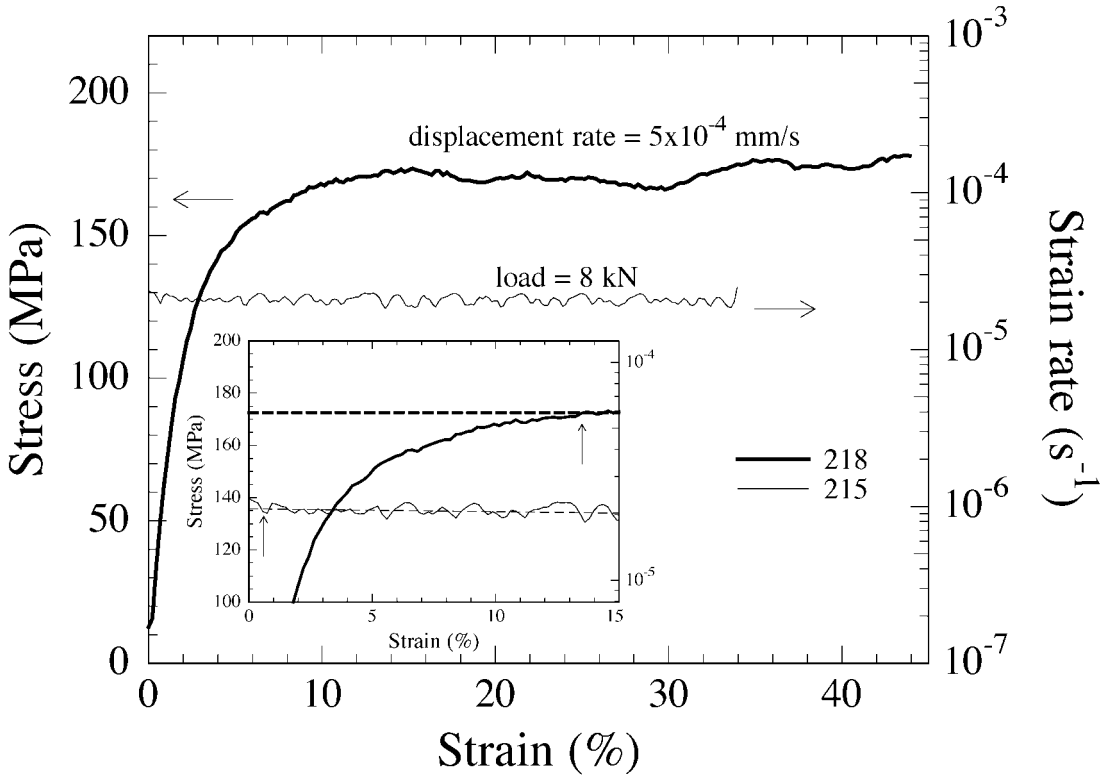

Fig. 7. Stress or strain rate vs strain for samples of lherzolite deformed at constant displacement rate or constant load, respectively, at $P = 300$ MPa. For the sample (218) deformed at constant displacement rate, $T = 1498$ K and $\varphi \approx 0{\cdot}04$. For the sample (215) deformed at constant load, $T = 1473$ K and $\varphi \approx 0{\cdot}03$. The data for both experiments were fitted with a smoothed spline function to eliminate fluctuations caused by electronic noise introduced during data acquisition. For the constant load experiment, oscillations occur because the strain rates are instantaneous values derived from the derivative of the displacement curve at each time step. The subplot highlights the differences between the data obtained from the two types of tests.

boundary diffusivity calculated from the Coble creep equation with values published for grain boundary diffusion of the constituent species of olivine. Substituting results from creep of subsolidus lherzolite and melt-free olivine at 1373 K, shown in Fig. 2, into the Coble creep equation, we estimate that the product of the grain boundary diffusivity, D^{gb}, and the boundary width, δ, is $D^{gb}\delta \approx 7{\cdot}4 \pm 2{\cdot}0 \times 10^{-23}$ and $7{\cdot}3 \pm 4{\cdot}0 \times 10^{-23}\,m^3/s$ for lherzolite and olivine, respectively. Consequently, deformation of lherzolite may be rate limited by diffusion of the same species along olivine grain boundaries. Hirth & Kohlstedt (1995*a*) concluded that deformation in their nominally melt-free olivine aggregates was rate limited by grain boundary diffusion of silicon based on the lack of correlation between their creep data and the limited number of published values for grain boundary diffusivity of oxygen and metal species in olivine.

In the diffusional creep regime, deformation is rate limited by diffusion of the slowest species along its fastest path. For lherzolite, available paths include pyroxene grain boundaries and olivine–pyroxene phase boundaries, as well as the olivine grain boundaries considered by Hirth & Kohlstedt (1995*a*). The grain boundary diffusivity for silicon in enstatite is

$$\bar{D}^{gb}_{Si}\delta = (3{\cdot}3 \pm 3{\cdot}0) \times 10^{-10} e^{-400 \pm 65/RT} m^3/s \quad (6)$$

based on the kinetics of the solid-state reaction of quartz and olivine to produce polycrystalline enstatite (Fisler *et al.*, 1997). [The pre-exponential term quoted by Fisler *et al.* (1997) of $(3{\cdot}3 \pm 3{\cdot}0) \times 10^{-9}\,m^3/s$ is corrected here to $(3{\cdot}3 \pm 3{\cdot}0) \times 10^{-10}\,m^3/s$ to fit the effective diffusivities reported in their fig. 6 using their reported average grain size of 0·25 μm assuming that their equation (7) correctly describes the solid-state reaction process.] At 1373 K, their result yields $1{\cdot}3 \times 10^{-26} \leq \bar{D}^{gb}_{Si}\delta \leq 5{\cdot}4 \times 10^{-24} m^3/s$ if the coupled errors in the pre-exponential and activation energy terms are considered. Based on the final position of a platinum marker placed between the two halves of the reaction couple, Fisler *et al.* concluded that the growth rate of the enstatite layer is limited by grain boundary diffusion of silicon with iron and magnesium being essentially immobile, that is, with $D_{Me} \ll D_{Si} \ll D_O$. Therefore, their results predict that, if the diffusional

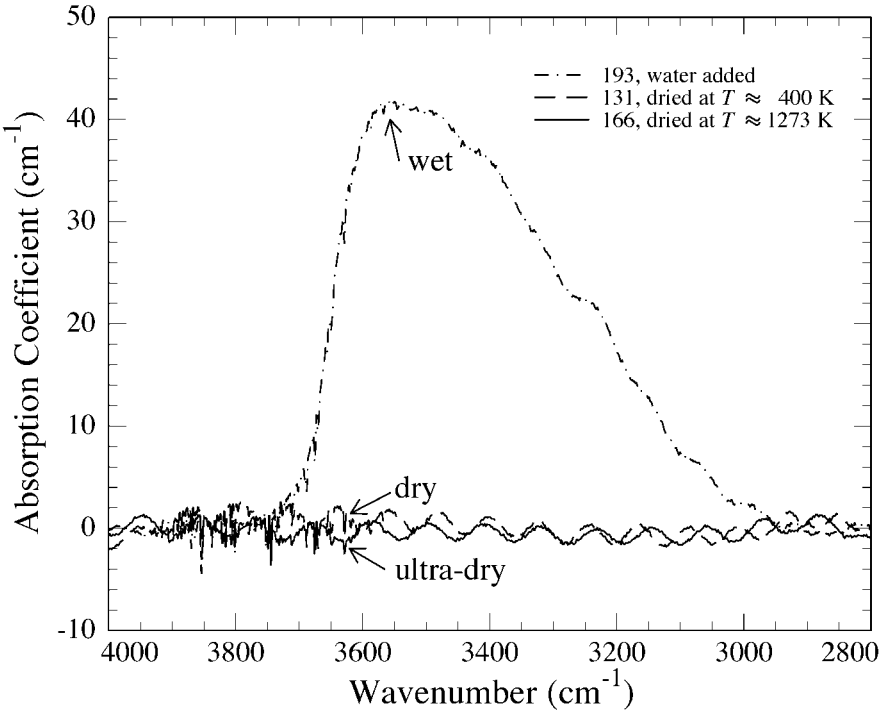

Fig. 8. Absorption coefficient vs wave number determined from unpolarized FTIR spectra for three samples of lherzolite. Each spectrum was obtained from an area with a diameter of ~100 μm. The upper spectrum labeled 'wet' is the absorption coefficient for a sample with water added prior to deformation and corresponds to an OH content of >300 H/10^6Si. The spectrum labeled 'dry' yields an OH content of ≤30 H/10^6Si for a sample dried after hot-press in a vacuum drying oven at 413 K, and the spectrum labeled 'ultra-dry' yields ≤10 H/10^6Si for a sample dried in a controlled atmosphere furnace at 1273 K. Because the samples were ~30 μm thick, sinusoidal oscillations in the FTIR spectra result from light reflected from the two surfaces of the sample.

creep rate in lherzolite is limited by grain boundary diffusion of iron and magnesium along enstatite grain boundaries, then the estimated rate will be more than an order of magnitude slower than that determined by our creep data. However, given the minimal amount of data available on grain boundary diffusion in olivine and pyroxene and the added complication of phase boundaries in the case of lherzolite, it is premature to draw any firm conclusions regarding identification of the rate-limiting species for diffusional creep of lherzolite.

The results of our creep experiments on partially molten lherzolite indicate that the strain rate enhancement in the diffusional creep regime as a result of the presence of melt is slightly less pronounced than the enhancement observed by Hirth & Kohlstedt (1995*a*). For the diffusional creep data for lherzolite in Fig. 10, strain rate increases by a factor of 10 with an increase in melt fraction from $\varphi = 0{\cdot}00$ to $\varphi = 0{\cdot}10$, whereas for the diffusional creep flow law for olivine plus basalt in the same figure, the strain rate increases by a factor of 20 over the same range in melt fraction (Hirth & Kohlstedt, 2003). The creep results for lherzolite are consistent with an exponential dependence of strain rate on melt fraction as expressed in equation (2) with $\alpha_{diff} = 21$. This exponential dependence of creep rate on melt fraction is also evidenced by the change in slope for lherzolite at temperatures above the solidus observed in the Arrhenius plots of Fig. 6a and b. The magnitude of the difference observed between creep of partially molten lherzolite and creep of olivine plus basalt shown in Fig. 10 for a melt fraction of 0·10 is reflected in the difference in the value of $\alpha_{diff} = 25$–30, reported by Mei & Kohlstedt (2000) and Hirth & Kohlstedt (2003) for dry olivine plus basalt, and the value of $\alpha_{diff} = 21$ reported here for lherzolite.

The influence of melt on deformation of olivine in the diffusional creep regime has been discussed by Hirth & Kohlstedt (1995*a*) in terms of the model of Cooper & Kohlstedt (1986). This model predicts strain rate enhancement as a result of the presence of melt, based on an isotropic distribution of melt in all of the three- and four-grain junctions of the fine-grained olivine aggregate. The resulting strain rate enhancement owing to the presence of melt is a consequence of the shortening of the grain boundary diffusive path length, because diffusion is faster through the melt phase, and of the stress increase associated with reduced grain-to-grain contact area. Both effects, which have the same geometrical form, increase with increasing melt

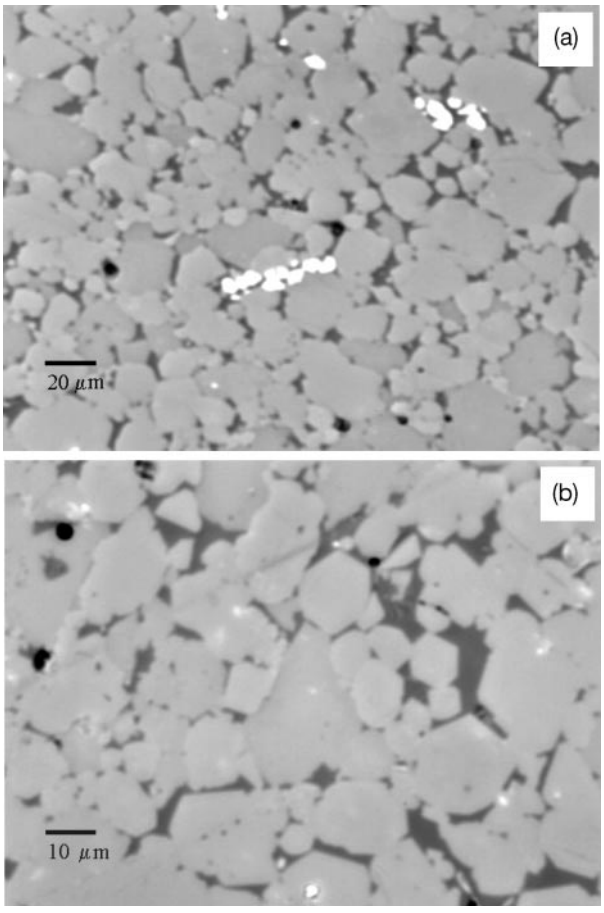

Fig. 9. Reflected light micrographs of a lherzolite sample (259) deformed at 1573 K. Scale bar represents 20 μm in (a), and 10 μm in (b). It is difficult to distinguish the mineral phases present; however, the olivine grains are generally lighter gray and the pyroxenes darker gray. The bright white grains in (a) are spinel and the darkest gray or black is melt. The melt fraction is $\varphi \approx 0{\cdot}10$. Melt is present in most of the junctions with at least one olivine grain present and along many of the olivine–olivine grain boundaries as well as some pyroxene–olivine phase boundaries. Melt pockets visible in (a) and (b) are aligned 15–20° to the maximum principal stress.

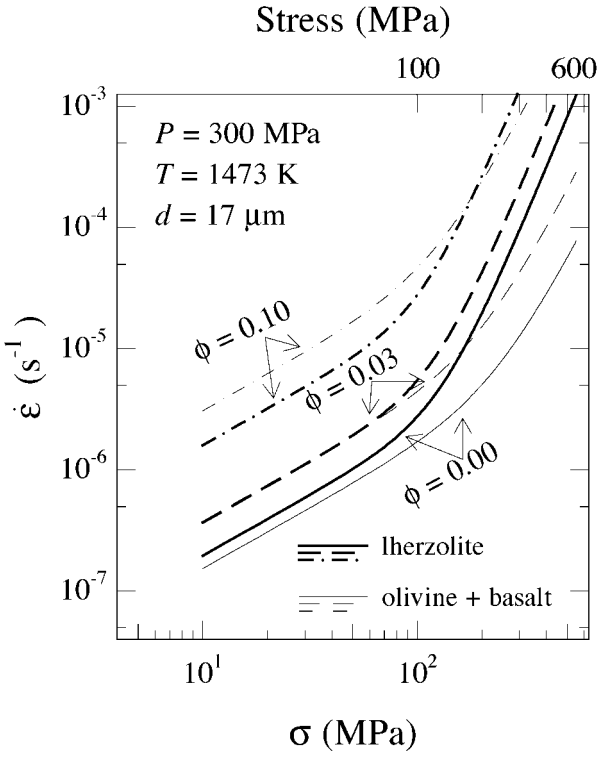

Fig. 10. Strain rate vs differential stress for lherzolite and olivine plus basalt at three melt fractions based on the constitutive equations reported here and by Hirth & Kohlstedt (2003), respectively. The difference in the change in strength of the two materials with increasing melt fraction should be noted. Melt-free olivine is stronger than lherzolite in both the diffusional and the dislocation creep regimes, but olivine plus basalt is dramatically weaker than partially molten lherzolite in the diffusional creep regime at a melt fraction of $\varphi = 0{\cdot}10$.

fraction and decreasing dihedral angle. Hirth & Kohlstedt (1995*a*) argued that the model adequately predicted the observed strain rates for melt fractions of $\varphi \leq 0{\cdot}05$ but significantly underestimated the dependence of strain rate on melt fraction for $\varphi > 0{\cdot}05$. The primary reason for the failure of this model to predict the observed enhancement in strain rate at the higher melt fractions appears to be the presence of melt along a significant fraction of grain boundaries, a consequence of the anisotropy of olivine–melt interfacial energy. The wetted boundaries provide rapid pathways for the diffusive transport of ionic species that are not accounted for in the isotropic model (Hirth & Kohlstedt, 1995*a*, 1995*b*).

In our deformed lherzolite samples, the distribution of melt is similar to that reported for the olivine–melt system (e.g. Daines & Kohlstedt, 1997; Zimmerman *et al.*, 1999). However, because our samples contain ~25 vol. % orthopyroxene and ~10 vol. % clinopyroxene, the fraction of grain boundaries completely wetted by melt increases more slowly with increasing melt fraction than reported for olivine plus basalt (Hirth & Kohlstedt, 1995*a*; Mei & Kohlstedt, 2000). This difference in wetting behavior may explain the difference in values of α_{diff} determined for the two systems. We observe melt in our lherzolite samples in almost all of the three- and four-grain junctions bordered by at least one olivine grain but not in junctions bordered entirely by pyroxene. Melt is also absent from three-grain junctions that are bordered by two clinopyroxene grains; however, very few of these junctions are present because of the low volume percentage of clinopyroxene in the sample. Melt is present only along grain or phase boundaries bordered either by two olivine grains or by an olivine and an orthopyroxene grain.

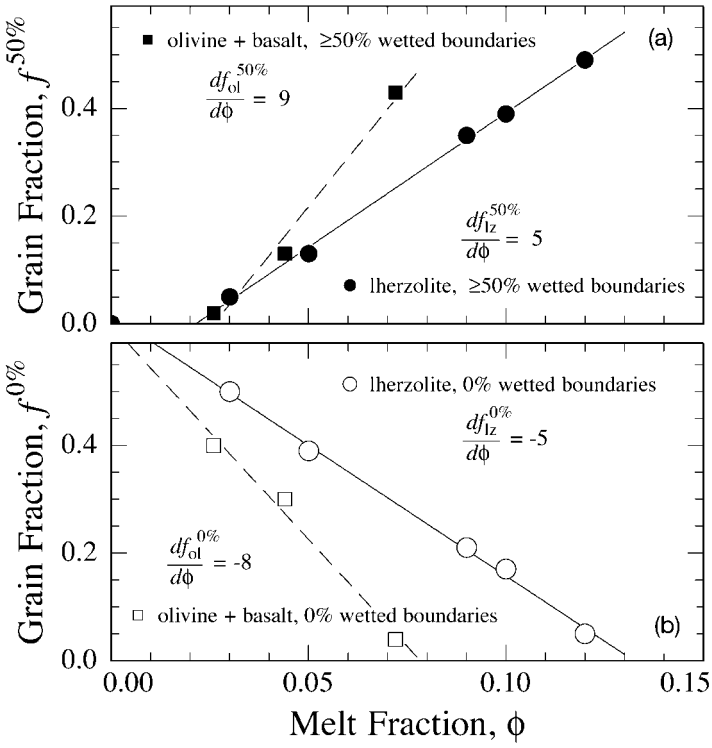

Fig. 11. (a) The fraction of grains with >50% of their boundaries wetted by melt vs melt fraction for lherzolite and olivine. (b) The fraction of grains with no boundaries wetted by melt vs melt fraction for lherzolite and olivine. The differences in the slopes are reflected in differences in strain rate dependence on melt fraction observed for the two systems.

In contrast, Toramaru & Fujii (1986) reported that melt is stable only along three-grain edges bordered entirely by olivine grains and in four-grain corners that contain at least three olivine grains for a hydrostatically annealed spinel lherzolite with 58 vol. % olivine, 25 vol. % orthopyroxene and 15 vol. % clinopyroxene. However, they observed melt in triple junctions with two olivine grains and even in triple junctions with just one olivine grain present, although they reported a more frequent occurrence of melt-free junctions with pyroxenes present. They measured a median value of 49° for the dihedral angle of olivine–olivine–melt junctions, which is nearly 30° larger than the value observed by Waff & Bulau (1982) for the same type of boundaries under similar temperature and pressure conditions. Differences in melt chemistry may account for the apparent differences in solid–liquid interfacial energies among the various studies performed under hydrostatic conditions (Beeman & Kohlstedt, 1993). In their estimate of the amount of melt required to maintain connectivity of the melt phase, Toramaru & Fujii (1986) found that the modal percentage of olivine and the relative grain size of the phases were the most important factors in determining connectivity of melt.

Although the distribution of melt that we observe in our samples is different from that reported by Toramaru & Fujii (1986), we can use a similar approach to estimate the number of grain boundaries likely to contain melt as a function of modal portion of olivine and grain size. Because melt occurs only along boundaries that have at least one olivine grain present, we estimate ~20% reduction in the number of boundaries likely to be wetted by melt as a result of the presence of ~35 vol. % pyroxene in our samples. This estimate depends critically on the relative grain size of the olivine and pyroxene grains; the percentage of wetted boundaries will increase (decrease) with increasing (decreasing) olivine grain size.

At a fixed melt fraction in a rock with an interconnected network of melt tubules and some wetted boundaries, melt excluded from pyroxene–pyroxene boundaries must distribute along boundaries that are more energetically favorable. In lherzolite, these boundaries include olivine–olivine and olivine–orthopyroxene boundaries as well as three-grain edges and four-grain corners with at least one olivine grain present. As illustrated in Fig. 11, we observe a linear increase in the number of grains with over half of their boundaries wetted by melt, from ~0·05 at $\varphi \approx 0{\cdot}03$ to ~0·4 at $\varphi \approx 0{\cdot}10$; Hirth & Kohlstedt (1995*a*) reported a more abrupt increase with increasing melt fraction, reaching ~0·4 by $\varphi \approx 0{\cdot}07$. The fraction of

grains with melt-free boundaries decreases linearly with increasing melt fraction in our lherzolite samples from ~0·5 for $\varphi \approx 0{\cdot}03$ to ~0·05 for $\varphi \approx 0{\cdot}12$ compared with a somewhat more rapid decrease in the fraction of grains with no wetted boundaries in olivine plus basalt samples with $0{\cdot}02 \leq \varphi \leq 0{\cdot}07$ (Hirth & Kohlstedt, 1995*a*). This difference may reflect a difference in melt chemistry and the distribution of interfacial energies for three solid phases and a melt phase, or it may reflect a difference in the distribution of grain sizes (e.g. Beeman & Kohlstedt, 1993). As melt fraction is increased, melt is not merely accommodated by increasing the size of the triple junction tubules but rather is stored in grain boundaries. Faul (1997) reported that, for $\varphi \geq 0{\cdot}02$, melt pockets along grain boundaries interconnect causing a substantial increase in permeability, consistent with the dramatic increase in strain rate that we observe at higher melt fractions.

The observed exponential dependence of strain rate on melt fraction as expressed in equation (2) cannot be accounted for by existing models based on an isotropic distribution of melt. The difference in the strain rate enhancement observed for olivine plus basalt and for partially molten lherzolite can be accounted for by the larger number of grains without melt along any boundaries and the reduced number of grains with >50% of boundaries with melt. To investigate the observed strain rate enhancement, models based on both isotropic and anisotropic distributions of melt in partially molten samples rely on reduction of diffusive grain boundary path length, associated with enhanced diffusion rates through the melt phase as well as modest increases in local stress concentrations. Comparison of the Cooper & Kohlstedt (1986) model for strain rate enhancement as a result of the presence of melt and the exponential dependence observed in this study, and that reported by Kelemen *et al.* (1997) and Mei & Kohlstedt (2002), are shown in Fig. 12 for diffusional creep. The enhancement in strain rate as a result of the presence of melt increases with decreasing dihedral angle in the Cooper & Kohlstedt (1986) model; a reduction in the dihedral angle from the observed value of ~38° to a value of <15° would be required to achieve the strain rate enhancement observed in this study for a sample with $\varphi = 0{\cdot}1$. Even taking into account the range of $20° < \theta < 50°$ reported for dihedral angles at olivine–basalt–olivine junctions in peridotites (Waff & Bulau, 1982; Toramaru & Fujii, 1986), the model still underestimates the effect of melt on strain rate at higher melt fractions.

As previously noted, the rate-limiting step in the deformation process remains transport along melt-free interfaces (e.g. Cooper *et al.*, 1989; Hirth & Kohlstedt, 1995*a*). Contrary to the results of Drury & Fitz Gerald (1996), recent high-resolution transmission electron microscopy (TEM) and analytical TEM observations of partially molten peridotites reveal that very thin films (10 nm) are not present at grain boundaries, although segregation of incompatible elements such as Ca and Al to olivine grain boundaries is pronounced (Hiraga *et al.*, 2002). However, relatively thick films of melt (~1 μm) line a significant fraction of the grain–grain interfaces. It is the presence of these thick melt films that increases the length of short-circuit diffusion path beyond that considered by Cooper & Kohlstedt (1986) and Cooper *et al.* (1989); that is, diffusion through these relatively thick melt films is much faster than through melt-free interfaces. Hence, diffusional deformation remains rate-limited by diffusion through melt-free grain boundaries, whereas the rate of deformation is enhanced by short-circuit diffusion through the melt-filled two-, three- and four-grain junctions. Finally, it should be noted that there is no evidence for melt wetting of all of the boundaries as reported by Jin *et al.* (1994).

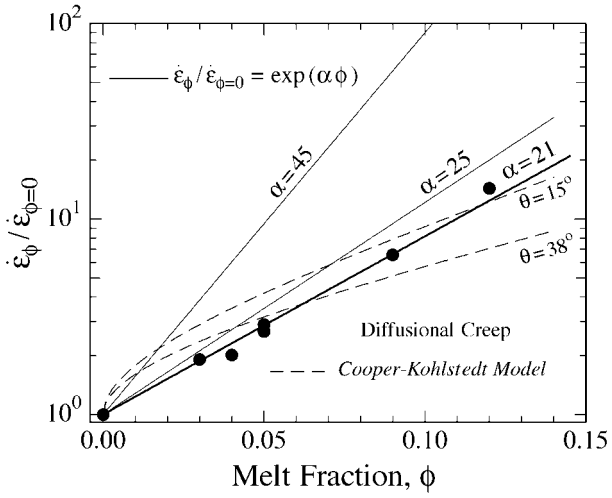

Fig. 12. Plot of strain rate enhancement in diffusional creep vs melt fraction. The strain rate enhancement is determined by normalizing the average strain rate for lherzolite samples at a given melt fraction by the average strain rate of subsolidus lherzolite deformed at the same stress and extrapolated to the same temperature. The dashed lines represent the strain rate enhancement predicted by the model of Cooper & Kohlstedt (1986) for several values of dihedral angle θ. The lherzolite data are fitted to an exponential dependence of strain rate on melt fraction with a value of $\alpha = 21$. The exponential relationships found by Kelemen *et al.* (1997) with $\alpha = 45$ and that for wet olivine plus basalt of Mei & Kohlstedt (2000) with $\alpha = 25$ are shown for comparison. The lower value of α determined in this study may reflect the fact that fewer grain boundaries are wetted by melt in the lherzolite samples than in the olivine plus basalt samples as a result of the high modal percentage of pyroxenes in the former. The model of Cooper & Kohlstedt (1986) with a typical dihedral angle of $\theta = 38°$ satisfactorily describes the influence of melt on strain rate determined experimentally for melt fractions of less than ~0·07 but underestimates the strain rate enhancement at higher melt fractions.

Transition to dislocation creep

The comparison in Fig. 10 of our constitutive equation for creep of lherzolite samples with the constitutive equation for creep of olivine and olivine–basalt aggregates (Hirth & Kohlstedt, 2003) indicates that the transition from diffusional to dislocation creep takes place near 100 MPa for both types of materials at $T = 1473$ K with $d = 17$ μm. At low melt fractions, the lherzolite samples are somewhat weaker than the olivine–basalt aggregates. This difference in strength decreases with increasing melt fraction; consistent with the observation that α_{disl} is smaller for the former than for the latter.

If these constitutive equations are extrapolated to mantle conditions including $T = 1723$ K (i.e. a depth of 200 km with a potential temperature of 1623 K, that is, 1350°C) and $d = 3$ mm, then, as illustrated in Fig. 13, lherzolite is stronger than olivine and olivine plus basalt for differential stresses between 0·1 and 10 MPa. [In this extrapolation, we have assumed that any increase in strength that occurs with increasing pressure is approximately offset by a decrease in strength owing to the presence of water (Hirth & Kohlstedt, 1996; Hirth & Kohlstedt, 2003).] Under these conditions, the transition between diffusional and dislocation creep occurs between 0·1 and 0·5 MPa.

As in the diffusion creep regime, the strain rate of partially molten lherzolite in the dislocation creep regime also increases approximately exponentially with increasing melt fraction, in this case with $\alpha_{disl} \approx 27$. In the dislocation creep regime, Hirth & Kohlstedt (1995*b*) rationalized the unexpectedly large enhancement in strain rate resulting from the presence of melt by modifying the stress enhancement component in the Cooper–Kohlstedt model (Cooper & Kohlstedt, 1986; Cooper *et al*., 1989). This approach results in an amplification of the stress enhancement term to the power $n_{disl} \approx 4{\cdot}3$. It should be noted that the observed strain rate enhancement is much larger than the factor of ~1·2 predicted by analytical models based on stress enhancement effects of inclusions (Chen & Argon, 1979; Hwang & Chen, 1990).

It is also interesting to note in Figs 10 and 13 that, as melt fraction is increased, the importance of dislocation creep relative to diffusional creep increases. Although this observation may be counter-intuitive, it is consistent with the observation that $\alpha_{disl} > \alpha_{diff}$.

Further implications

The similarity between our creep results for lherzolite and the results for olivine of Hirth & Kohlstedt (1995*a*, 1995*b*) in both the diffusional and dislocation creep regimes demonstrates that the addition of ~40% pyroxene to an olivine aggregate does not dramatically influence the strength of the resulting rock. This observation is consistent with creep results for olivine plus orthopyroxene, which show only about a factor of two difference in rate for different mole fractions of orthopyroxene and olivine (Hitchings *et al*., 1989), and with deformation results for synthetic very fine-grained (1–2 μm) forsterite-plus-enstatite material under wet conditions (McDonnell *et al*., 2000), which reveal no significant difference in flow strength up to 20 vol. % enstatite. Our results are also congruent with creep results for clinopyroxene samples, which deform at approximately the same strain rates as those reported in our study for similar conditions of T, P, d and σ (Bystricky & Mackwell, 2001). Wheeler (1992) has argued that the presence of phase boundaries should enhance diffusion rates in polymineralic rocks; however, the additional phase boundaries do not appear to have a significant effect on the deformation rate of lherzolite. Although the rates of deformation in our fine-grained lherzolite samples are similar to those determined for fine-grained olivine and olivine–basalt aggregates, the stress exponent and activation energy are higher for the former than for the latter in the dislocation creep regime. This result is broadly consistent with the result that the values of n and Q are higher

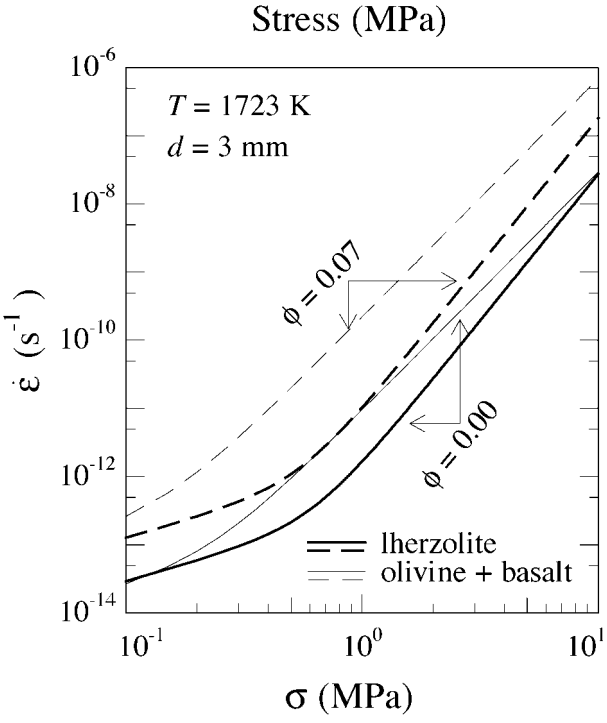

Fig. 13. Strain rate vs differential stress based on the constitutive equations for lherzolite and olivine–basalt samples with $\varphi = 0{\cdot}00$ and $\varphi = 0{\cdot}07$ extrapolated to a mantle temperature of 1723 K and grain size of 3 mm assuming that the strengthening effect of increasing pressure (depth) is roughly offset by the weakening effect of water.

for deformation of pyroxene (Bystricky & Mackwell, 2001) than for creep of olivine (Hirth & Kohlstedt, 1995*b*).

If, as is often reported, the average melt fraction near the mid-ocean ridge basalt (MORB) source region beneath a mid-ocean ridge is 1 vol. %, then our results imply that melt will reduce the viscosity of partially molten mantle rocks by $\leq$20%. However, recent laboratory experiments demonstrate that, during large-strain deformation of partially molten rocks, melt can segregate into melt-rich regions (Holtzman *et al.*, 2003). These relatively narrow channels contain 10 or more times the amount of melt found in the surrounding rock. Hence, they provide high-permeability paths that would facilitate rapid transport of melt to the Earth's surface. In addition, these melt-enriched channels will be significantly weaker than the surrounding mantle, such that deformation would localize on them, producing shear zones. Similar structures reflecting the juxtaposition of melt-rich regions with shear zones have been observed in ophiolites (Kelemen & Dick, 1995; Dijkstra *et al.*, 2002).

CONCLUSIONS

Our deformation experiments conducted on fine-grained lherzolite at subsolidus and hypersolidus temperatures under dry conditions and strain rates in the range of $\sim 10^{-7}$ to $10^{-3}\,s^{-1}$ reveal a transition from diffusional creep to dislocation creep at a differential stress of $\sigma \approx 100$ MPa for a grain size of $d \approx 20\,\mu m$ and melt fractions of $0 \leq \varphi \leq 0{\cdot}1$. For small values of φ (0–0·02), extrapolation to mantle conditions using equation (5), with experimentally determined values from Table 2, predicts a transition between diffusional creep and dislocation creep at $\sigma \approx 2$ MPa (viscosity of 2×10^{17} Pa s) for $d = 1$ mm and at $\sigma \approx 0{\cdot}2$ MPa (viscosity of 2×10^{20} Pa s) for $d = 10$ mm. This behavior is similar to that reported for olivine plus basaltic melt, indicating a small effect of the $\sim$40 vol. % pyroxene in our samples.

The results also indicate a substantial reduction in upper-mantle viscosity of $\sim$10 for $\varphi = 0{\cdot}10$ but a modest reduction of $\sim 1{\cdot}2$ for $\varphi = 0{\cdot}01$. The approximately exponential dependences of strain rate on melt fraction with $\alpha \approx 21$ and 27 in the diffusional and dislocation creep regimes, respectively, cannot be accounted for by existing models based on an isotropic distribution of melt. The observed strain rate enhancement in diffusional creep can be accounted for by also considering the reduction in diffusion path length along melt-free boundaries associated with the presence of grain–grain interfaces containing melt, combined with related stress enhancement associated with anisotropic interfacial energies. In the dislocation creep regime, the strain rate enhancement observed with the addition of melt is qualitatively consistent with a stress enhancement caused by the replacement of grain or phase interfaces by melt.

ACKNOWLEDGEMENTS

Zhenmin Jin generously gave us the Damping lherzolite for use in our experiments. In the review process, David Mainprice, Ernie Rutter, and especially Chris Spiers provided valuable comments that led to significant improvements to this paper. Support from the National Science Foundation through grants EAR-0126277, INT-0123224 and OCE-0002463 is gratefully acknowledged, as well as a Graduate School Dissertation Fellowship from the University of Minnesota.

REFERENCES

Arzi, A. A. (1978). Critical phenomena in the rheology of partially melted rocks. *Tectonophysics* **44**, 173–184.

Ashby, M. F. & Verrall, R. A. (1973). Diffusion accommodated flow and superplasticity. *Acta Metallurgica* **21**, 149–163.

Bai, Q., Mackwell, S. J. & Kohlstedt, D. L. (1991). High-temperature creep of olivine single crystals: 1. Mechanical results for buffered samples. *Journal of Geophysical Research* **96**, 2441–2463.

Beeman, M. L. & Kohlstedt, D. L. (1993). Deformation of fine-grained aggregates of olivine plus melt at high temperatures and pressures. *Journal of Geophysical Research* **98**, 6443–6452.

Bell, D. R., Rossman, G. R., Maldener, J., Endisch, D. & Rauch, F. (2003). Hydroxide in olivine: a quantitative determination of the absolute amount and calibration of the IR spectrum. *Journal of Geophysical Research* **108**, 1029/2001JB000679.

Brace, W. F. & Riley, D. K. (1972). Static uniaxial deformation of 15 rocks to 30 kb. *International Journal of Rock Mechanics and Mining Sciences* **9**, 271–288.

Brook, R. J. (1976). Controlled grain growth. In: Wang, F. F. Y. (ed.) *Ceramic Fabrication Processes*. New York: Academic Press, pp. 331–365.

Bussod, G. Y. & Christie, J. M. (1991). Textural development and melt topology in spinel lherzolite experimentally deformed at hypersolidus conditions. *Journal of Petrology, Special Volume* 17–39.

Bystricky, M. & Mackwell, S. (2001). Creep of dry clinopyroxene aggregates. *Journal of Geophysical Research* **106**, 13443–13454.

Chen, I. W. & Argon, A. S. (1979). Grain boundary and interphase boundary sliding in power law creep. *Acta Metallurgica* **27**, 749–754.

Chopra, P. N. & Paterson, M. S. (1981). The experimental deformation of dunite. *Tectonophysics* **78**, 453–473.

Coble, R. L. (1963). A model for boundary-diffusion controlled creep in polycrystalline materials. *Journal of Applied Physics* **34**, 1679–1682.

Cooper, R. F. & Kohlstedt, D. L. (1984). Solution–precipitation enhanced creep of partially molten olivine–basalt aggregates during hot-pressing. *Tectonophysics* **107**, 207–233.

Cooper, R. F. & Kohlstedt, D. L. (1986). Rheology and structure of olivine–basalt partial melts. *Journal of Geophysical Research* **91**, 9315–9323.

Cooper, R. F., Kohlstedt, D. L. & Chyung, C. K. (1989). Solution–precipitation enhanced creep in solid–liquid aggregates

which display a non-zero dihedral angle. *Acta Metallurgica* **37**, 1759–1771.

Daines, M. J. & Kohlstedt, D. L. (1997). Influence of deformation on melt topology in peridotites. *Journal of Geophysical Research* **102**, 10257–10271.

Deer, W. A., Howie, R. A. & Zussman, J. (1992). *An Introduction to the Rock Forming Minerals*, 2nd edn. Harlow: Longman.

Dieter, G. E. (1976). *Mechanical Metallurgy*, 2nd edn. New York: McGraw–Hill.

Dijkstra, A. H., Drury, M. R. & Frijhoff, R. M. (2002). Microstructures and lattice fabrics in the Hilti mantle section (Oman Ophiolite): evidence for shear localization and melt weakening in the crust–mantle transition zone? *Journal of Geophysical Research* **107**, 1029/2001JB000458.

Drury, M. R. & Fitz Gerald, J. D. (1996). Grain boundary melt films in an experimentally deformed olivine–orthopyroxene rock: implications for melt distribution in upper mantle rocks. *Geophysical Research Letters* **23**, 701–704.

Evans, B. & Kohlstedt, D. L. (1995). Rheology of rocks. In: Ahrens, T. (ed.) *Rock Physics and Phase Relations: a Handbook of Physical Constants*. Washington, DC: American Geophysical Union, pp. 148–165.

Fan, D. & Chen, L.-Q. (1997). Diffusion-controlled grain growth in two-phase solids. *Acta mater.* **45**, 3297–3310.

Faul, U. H. D. (1997). Permeability of partial melts. *Journal of Geophysical Research* **102**, 10299–10311.

Faul, U. H. D., Toomey, R. & Waff, H. S. (1994). Intergranular basaltic melt is distributed in thin, elongated inclusions. *Geophysical Research Letters* **21**, 29–32.

Fisler, D. K., Mackwell, S. J. & Petsch, S. (1997). Grain boundary diffusion in enstatite. *Physics and Chemistry of Minerals* **24**, 264–273.

Gifkins, R. C. (1970). *Optical Microscopy of Metals*. New York: Elsevier.

Goetze, C. (1977). A brief summary of our present day understanding of the effect of volatiles and partial melt on the mechanical properties of the upper mantle. In: Manghnani, M. H. & Akimoto, S. (eds) *High-Pressure Research: Applications in Geophysics*. New York: Academic Press, pp. 3–23.

Goetze, C. (1978). The mechanisms of creep in olivine. *Philosophical Transactions of the Royal Society of London, Series A* **288**, 59–119.

Groves, G. W. & Kelly, A. (1968). Independent slip systems in crystals. *Philosophical Magazine* **8**, 877–887.

Hamilton, P. J., O'Nions, R. K., Bridgwater, D. & Nutman, A. (1983). Sm–Nd studies of Archean metasediments and metavolcanics from West Greenland and their implications for the Earth's early history. *Earth and Planetary Science Letters* **62**, 263–272.

Herring, C. (1950). Diffusional viscosity of a polycrystalline solid. *Journal of Applied Physics* **21**, 437–445.

Herring, C. (1951). Surface tension as a motivation for sintering. In: Kingston, W. E. (ed.) *The Physics of Powder Metallurgy*. New York: McGraw–Hill.

Hess, P. C. (1989). *Origins of Igneous Rocks*. Boston, MA: Harvard University Press, 336 pp.

Hiraga, T., Anderson, I. M., Zimmerman, M. E., Mei, S. & Kohlstedt, D. L. (2002). Structure and chemistry of grain boundaries in deformed olivine + basalt and partially molten lherzolite aggregates: evidence of melt-free grain boundaries. *Contributions to Mineralogy and Petrology* **144**, 163–175.

Hirth, G. & Kohlstedt, D. L. (1995*a*). Experimental constraints on the dynamics of the partially molten upper mantle: deformation in the diffusion creep regime. *Journal of Geophysical Research* **100**, 1981–2001.

Hirth, G. & Kohlstedt, D. L. (1995*b*). Experimental constraints on the dynamics of the partially molten upper mantle: deformation in the dislocation creep regime. *Journal of Geophysical Research* **100**, 15441–15449.

Hirth, G. & Kohlstedt, D. L. (1996). Water in the oceanic upper mantle: implications for rheology, melt extraction and the evolution of the lithosphere. *Earth and Planetary Science Letters* **144**, 93–108.

Hirth, G. & Kohlstedt, D. L. (2003). Rheology of the upper mantle and the mantle wedge: a view from the experimentalists. In: Plank, T. & Hirschmann, M. M. (eds) *Margins: Theoretical and Experimental Earth Science Series. Volume II: Inside the Subduction Factory*. New York: Columbia University Press, in press.

Hitchings, R. S., Paterson, M. S. & Bitmead, J. (1989). Effects of iron and magnetite additions in olivine–pyroxene rheology. *Physics of the Earth and Planetary Interiors* **55**, 277–291.

Holtzman, B. K., Groebner, N. J., Zimmerman, M. E., Ginsberg, S. B. & Kohlstedt, D. L. (2002). Deformation-driven melt segregation in partially molten rocks. *Geochemistry, Geophysics, Geosystems* **8607**, DOI: 10.1029/2001GC000258.

Hwang, C. & Chen, I.W. (1990). Effect of a liquid phase on superplasticity of 2-mol % Y_2O_3-stabilized tetragonal zirconia polycrystals. *Journal of the American Ceramics Society* **73**, 1626–1632.

Jin, Z. M., Green, H. W. & Zhou, Y. (1994). Melt topology during dynamic partial melting of mantle peridotite. *Nature* **372**, 164–167.

Karato, S. I. (1998). Effects of pressure on plastic deformation of polycrystalline solids: some geological applications. *Materials Research Society Symposium Proceedings* **499**, 3–14.

Kelemen, P. B. & Dick, H. J. (1995). Focused melt flow and localized deformation in the upper mantle: juxtaposition of replacive dunite and ductile shear zones in the Josephine peridotite, SW Oregon. *Journal of Geophysical Research* **100**, 423–438.

Kelemen, P. B., Hirth, G., Shimizu, N., Spiegelman, M. & Dick, H. J. B. (1997). A review of melt migration processes in the adiabatically upwelling mantle beneath oceanic spreading ridges. *Philosophical Transactions of the Royal Society of London, Series A* **355**, 283–318.

Kirby, S. H. (1983). Rheology of the lithosphere. *Reviews of Geophysics and Space Physics* **21**, 1458–1487.

Kirby, S. H. & Kronenberg, A. K. (1987). Rheology of the lithosphere: selected topics. *Reviews of Geophysics* **25**, 1219–1244.

Koga, K., Hauri, E., Hirschmann, M. & Bell, D. (2003). Hydrogen concentration analyses using SIMS and FTIR: comparison and calibration for nominally anhydrous minerals. *Geochemistry, Geophysics, Geosystems* **4**, 1019, DOI: 10.1029/2002GC000378.

Kohlstedt, D. L. (1992). Structure, rheology and permeability of partially molten rocks at low melt fractions. In: Phipps-Morgan, J., Blackman, D. K. & Sinton, J. M. (eds) *Mantle Flow and Melt Generation at Mid-Ocean Ridges. Geophysical Monograph, American Geophysical Union* **71**, 103–121.

Kohlstedt, D. L., Evans, B. & Mackwell, S. J. (1995). Laboratory constraints on the strength of the lithosphere. *Journal of Geophysical Research* **100**, 17587–17602.

Kohlstedt, D. L., Keppler, H. & Rubie, D. C. (1996). Solubility of water in the α, β and γ phases of $(Mg, Fe)_2SiO_4$. *Contributions to Mineralogy and Petrology* **123**, 345–357.

Langdon, T. C. (1975). Grain-boundary processes during creep. In: Li, J. C. M. & Mukherjee, A. K. (eds) *Rate Processes in Plastic*

Deformation of Materials. Metals Park, OH: American Society for Metals, pp. 410–433.

Langdon, T. G. (1994). A unified approach to grain boundary sliding in creep and superplasticity. *Acta Metallurgica Mater. Proceedings from the John E. Dorn Symposium, sponsored by the Flow and Fracture Activity of the Materials Science Division, American Society for Metals* **42**, 2437–2443.

Lifshitz, I. M. (1963). On the theory of diffusion–viscous flow of polycrystalline bodies. *Journal of Experimental and Theoretical Physics (USSR)* **44**, 1349–1367 (translated in *Soviet Physics JETP* **17**, 909–920).

McDonnell, R. D., Peach, C. J., van Roermund, H. L. M. & Spiers, C. J. (2000). Effect of varying enstatite content on the deformation of fine-grained synthetic peridotite under wet conditions. *Journal of Geophysical Research* **105**, 13535–13553.

Mei, S. & Kohlstedt, D. L. (2000). Influence of water on plastic deformation of olivine aggregates: 2. Dislocation creep regime. *Journal of Geophysical Research* **105**, 21471–21481.

Mei, S., Bai, W., Hiraga, T. & Kohlstedt, D. L. (2002). Influence of melt on the creep behavior of olivine–basalt aggregates under hydrous conditions. *Earth and Planetary Science Letters* **201**, 491–507.

Michael, P. (1988). The concentration, behavior and storage of H_2O in the suboceanic upper mantle: implications for mantle metasomatism. *Geochimica et Cosmochimica Acta* **52**, 555–566.

Nabarro, F. R. N. (1948). Deformation of crystals by the motion of single ions. *Report of a Conference on Strength of Solids (Bristol)*. London: The Physical Society (Great Britain), pp. 75–90.

Nabarro, F. R. N. (1967). Steady-state diffusional creep. *Philosophical Magazine* **16**, 231–237.

Parrish, D. K. & Gangi, A. F. (1981). A nonlinear least squares technique for determining multiple-mechanism, high-temperature creep flow laws. In: Carter, N. L., Friedman, M., Logan, J. M. & Stearns, D. W. (eds) *Mechanical Behavior of Crustal Rocks, The Handin Volume*. Washington, DC: American Geophysical Union, pp. 287–298.

Paterson, M. S. (1969). The ductility of rocks. In: Argon, A. S. (ed.) *Physics of Strength and Plasticity*. Cambridge, MA: MIT Press, pp. 377–392.

Paterson, M. S. (1978). *Experimental Rock Deformation: the Brittle Field*. Berlin: Springer.

Paterson, M. S. (1982). The determination of hydroxyl by infrared absorption in quartz, silicate glasses and similar materials. *Bulletin de Minéralogie* **105**, 20–29.

Paterson, M. S. (1990). Rock deformation experimentation. In: Duba, A. G., Durham, W. B., Handin, J. W. & Wang, H. F. (eds) *The Brittle–Ductile Transition in Rocks. Geophysical Monograph, American Geophysical Union* **56**, 187–194.

Raj, R. & Ashby, M. F. (1971). On grain boundary sliding and diffusional creep. *Metallurgical Transctions* **2**, 1113–1127.

Riley, G. N., Jr & Kohlstedt, D. L. (1991). Kinetics of melt migration in upper mantle-type rocks. *Earth and Planetary Science Letters* **105**, 500–521.

Ringwood, A. E. (1975). *Composition and Petrology of the Earth's Mantle*. New York: McGraw–Hill.

Stolper, E. M., Walker, D., Hager, B. H. & Hays, J. F. (1981). Melt segregation from partially molten source regions: the importance of melt density and source region size. *Journal of Geophysical Research* **86**, 6261–6271.

Toramaru, A. & Fujii, N. (1986). Connectivity of melt phase in a partially molten peridotite. *Journal of Geophysical Research* **91**, 9239–9252.

Tullis, J. A. (1979). High temperature deformation of rocks and minerals. *Reviews of Geophysics and Space Physics* **17**, 1137–1154.

Van der Wal, D. (1993). *Deformation Processes in Mantle Peridotites: with Emphasis on the Ronda Peridotite*. Utrecht: Faculteit Aardwetenschappen der Rijksununiversiteit Utrecht.

von Mises, R. (1928). Mechanik der plastichen Fomanderung von Kristallen. *Zeitschrift Angewandte Mathematik und Mechanik* **8**, 161.

Waff, H. S. & Bulau, J. R. (1979). Equilibrium fluid distribution in an ultramafic partial melt under hydrostatic stress conditions. *Journal of Geophysical Research* **84**, 6109–6114.

Waff, H. S. & Bulau, J. R. (1982). Experimental determination of near equilibrium textures in partially molten silicates at high pressure. In: Akimoto, S. & Manghnani, M. H. (eds) *High-Pressure Research in Geophysics, Advances in Earth and Planetary Sciences, 12*. Tokyo: Center for Academic Publications, pp. 229–236.

Waff, H. S. & Faul, U. H. (1992). Effects of crystalline anisotropy on fluid distribution in ultramafic partial melts. *Journal of Geophysical Research* **97**, 9003–9014.

Watson, E. B. (1982). Melt infiltration and magma evolution. *Geology* **10**, 236–240.

Webb, S. L. (1989). The elasticity of the upper mantle orthosilicates olivine and garnet to 3 GPa. *Physics and Chemistry of Minerals* **16**, 684–692.

Weertman, J. (1972). High temperature creep produced by dislocation motion. In: *J. E. Dorn Memorial Symposium, Cleveland, Ohio, October 17, 1972*.

Wendt, A. S., Mainprice, D., Rutter, E. & Wirth, R. (1998). A joint study of experimental deformation and experimentally induced microstructures of pretextured peridotites. *Journal of Geophysical Research* **103**, 18205–18221.

Wheeler, J. (1992). Importance of pressure solution and Coble creep in the deformation of polymineralic rocks. *Journal of Geophysical Research* **97**, 4579–4586.

Zimmerman, M. E., Zhang, S., Kohlstedt, D. L. & Karato, S. I. (1999). Melt distribution in mantle rocks deformed in shear. *Geophysical Research Letters* **26**, 1505–1508.

APPENDIX A: RELATIVE CONTRIBUTIONS OF DIFFUSIONAL AND DISLOCATION CREEP

In recent analyses of creep data, Bystricky & Mackwell (2001) and Hirth & Kohlstedt (2003) have pointed out that it is difficult with fine-grained samples to perform creep experiments that are far from the transition between diffusional and dislocation creep. However, experiments on such synthetic rock samples are essential as they provide constraints on flow in both creep regimes. With samples from coarser-grained natural rock specimens, creep experiments can explore deformation only in the dislocation creep regime, limiting the possibility of extrapolating from laboratory to geological conditions.

The approach generally taken in laboratory experiments on finer-grained samples is to access the diffusional creep regime by deforming at relatively low differential stresses and to explore the dislocation creep regime by deforming at relatively high differential stresses. This approach raises the question of the

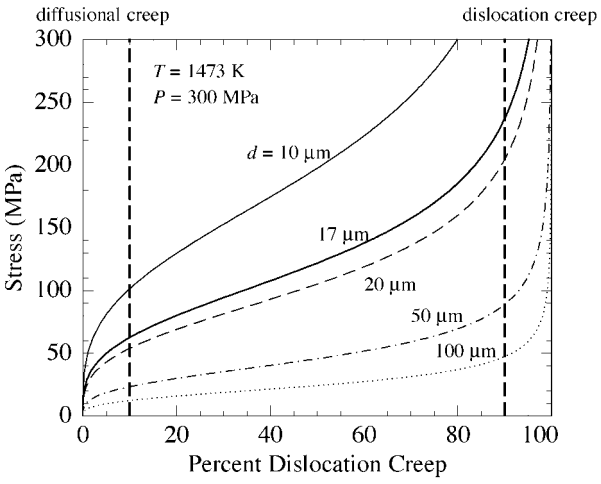

Fig. A1. Stress vs percent dislocation creep for a range of grain sizes at fixed temperature and pressure.

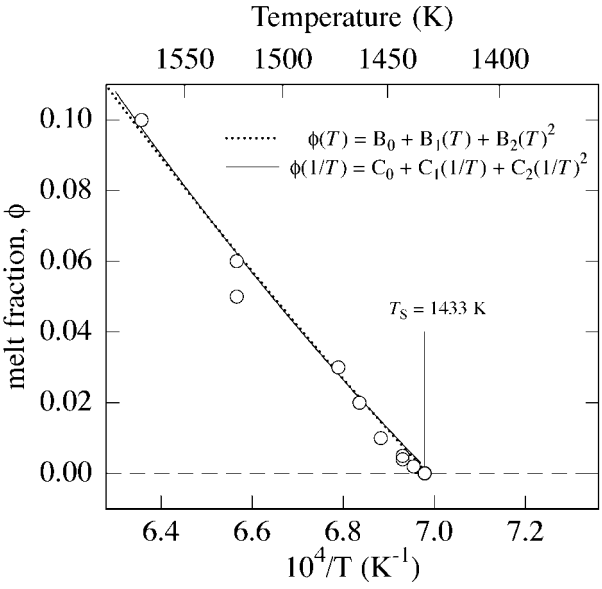

Fig. A2. Melt fraction vs inverse temperature for lherzolite samples quenched at the temperatures indicated by the open circles. For the limited temperature range explored in this study, the melt fraction is well described by a second-order polynomial fit in either T or $1/T$.

distinction between low and high differential stress. To address this point, we have plotted our constitutive equation for combined diffusional and dislocation creep in Fig. A1 in the form differential stress vs percent dislocation creep. By considering the measured (total) strain rate as the sum of the strain rate arising from diffusional creep plus the strain rate owing to dislocation creep, $\dot{\varepsilon}_{tot} = \dot{\varepsilon}_{diff} + \dot{\varepsilon}_{disl}$, we calculated the percent dislocation creep as $(\dot{\varepsilon}_{disl}/\dot{\varepsilon}_{tot}) \times 100$ for a range of grain sizes at a fixed temperature and pressure. As is illustrated in Fig. A1, for a grain size of 17 μm (a typical value for our experiments) dislocation creep contributes ≥90% to the measured strain rate only at differential stresses greater than ~240 MPa. Similarly, for the same grain size, diffusional creep contributes 90% to the total strain rate only at differential stresses of 60 MPa. Hence, it is important that care be exercised in analyzing experimental creep data, to insure that the diffusional and dislocation contributions to the measured strain rate are properly identified.

APPENDIX B: DEPENDENCE OF MELT FRACTION ON TEMPERATURE

To determine α and Q_{ss}, we parameterized our measurements of melt fraction as a function of temperature and as a function of inverse temperature for our lherzolite samples. The change in melt fraction with temperature shown in Fig. A2 was determined from optical micrographs of samples quenched at several temperatures between 1373 and 1573 K. The resulting expressions for the dependence of melt fraction on temperature are (1) $\varphi = B_0 + B_1 T + B_2 T^2$ with $B_0 = -1{\cdot}1$, $B_1 = 8{\cdot}0 \times 10^{-4}\,\mathrm{K}^{-1}$ and $B_2 = -3{\cdot}9 \times 10^{-8}\,\mathrm{K}^{-2}$ and (2) $\varphi = C_0 + C_1/T + C_2/T_2$ with $C_0 = 1{\cdot}37$, $C_1 = -2{\cdot}42 \times 10^3\,\mathrm{K}^1$ and $C_2 = 6{\cdot}65 \times 10^5\,\mathrm{K}^2$ determined from least-squares fits to the data.